PHYSICAL IMPLICATIONS OF CHARACTERISTIC SPEEDS AND WAVEFORMS OF RAILS ON ELASTIC FOUNDATIONS

A Thesis presented to
the Faculty of the Graduate School
University of Missouri - Columbia

In Partial Fulfillment
of the Requirements for the Degree
Master of Science

---

by
CORY A. KAUFMAN
Dr. P. Frank Pai, Thesis Supervisor

MAY 2012

The undersigned, appointed by the Dean of the Graduate School, have examined the thesis entitled

PHYSICAL IMPLICATIONS OF CHARACTERISTIC SPEEDS AND WAVEFORMS OF RAILS ON ELASTIC FOUNDATIONS

presented by Cory A. Kaufman,

a candidate for the degree of Master of Science in Mechanical Engineering,

and hereby certify that, in their opinion, it is worthy of acceptance.

Professor P. Frank Pai

Professor Zaichun Feng

Professor Annette Sobel

ACKNOWLEDGEMENTS

I would like to start by thanking my family who has supported all the decisions I have made and helped financially make it possible for me to attend the University of Missouri. Second, I need to acknowledge the intelligence and guidance of my graduate thesis supervisor Dr. P. Frank Pai. His patience and teachings during my tenure at Mizzou have prompted a profound growing in myself both intellectually and professionally. In addition, I extend thanks to Dr. Roger Fales, Dr. Gary Solbrekken, and Dr. Zaichun Feng who have at some point heavily influenced my studies and research in engineering. My successes are attributed in no small part to all of these people who without their combination of support and direction I would not be where I am today.

I would also like to thank Dr. Annette Sobel who served as the University of Missouri Railgun Program Director, the United States Navy as well as the Office of Naval Research for providing funding towards our research and the forward progression of electromagnetic railguns, and the Institute for Advanced Technology for providing us with their experimental setups and data. It really was a privilege and a pleasure working in conjunction with so many great minds.

TABLE OF CONTENTS

LIST OF FIGURES

Figure **Page**

LIST OF FIGURES (continued)

Figure **Page**

LIST OF FIGURES (continued)

Figure **Page**

PHYSICAL IMPLICATIONS OF CHARACTERISTIC SPEEDS AND WAVEFORMS OF RAILS ON ELASTIC FOUNDATIONS

Cory A. Kaufman
Dr. P. Frank Pai, Thesis Supervisor

ABSTRACT

When a moving load is applied on an elastic rail with an elastic insulator, wave propagation can occur and become problematic after certain characteristic speeds are reached. Research of these waveforms and characteristic speeds is specifically applicable for understanding electromagnetic railgun dynamics. There are three characteristic speeds for an elastic rail on an elastic foundation: critical, shear, and bar speeds - critical speed being the slowest and the first speed reached by the armature, followed by shear and bar speeds respectively. Studying these speeds and the deformations associated with them is essential in understanding the dynamics and damage effects of rail-armature interaction.

One dimensional analysis of a quasi-stationary load moving along an infinite beam on an elastic foundation reveals different waveforms between these characteristic speeds. Before the critical speed there is a standing wave on the rail. When the moving load resonates with the standing wave at a critical excitation frequency this is called the critical speed. After the critical speed, elastic propagation of waves occurs in front of and behind the load causing a bumpy path for the load as it moves. In the case of a railgun, the extremely high forces along with an uneven path can cause significant damage to the rail as well as large mass loss in the armature. As the moving load speed approaches the shear speed, the wave lengths in front of the load become shorter and shorter until the point at which propagating waves no longer exist in front of the load, which is known as the shear speed. Between the shear and bar speeds, a single exponentially decaying, non-oscillating wave exists in front of the load, but backward waves continue to grow in amplitude and wavelength. Once the bar speed is reached, no transverse elastic waves can be pushed faster than the load, therefore no waves exist in front of the moving load, but significant backward waves can cause serious impacts since in reality the load has

multiple points in contact with the rail. Also important to note is that a backward longitudinal wave known as the bar-mode exists, and the rail acts like a rigid bar resonating with the elastic foundation after the bar speed.

Furthermore, two-dimensional finite element analyses of rail cross-sectional planes can reveal the geometrical mode shapes and their longitudinal wave propagation within the rail. There are six relevant modes for a rail cross-sectional plane: bending with respect to three orthogonal directions, a longitudinal wave (bar-mode), a torsional wave, and a shear wave. Under different excitation frequencies the magnitudes and propagation speeds of these modes change. With an elastic foundation we show that some of these modes have cut-on speeds, which result in different critical velocities in the rail-armature system. Moreover, the relationship between the critical speeds and different geometrical, thermal, and insulator properties are examined. Understanding the waveforms and mode shapes of a typical rail-foundation is the goal of this research. With a firm understanding of the dynamics and accurate modeling, various computational scenarios are investigated to find a feasible solution that can reduce the damaging interaction between the armature and rails.

CHAPTER 1
INTRODUCTION

1.1 Background

Large, rapidly moving loads have great effects on the dynamics of structures in contact with such loading. Some examples of these systems include train railways and airport runways. Serious vibrations and induced stresses can occur that are much greater than static stresses. Typical research is only done around the critical speed, however in higher speed applications more characteristic speeds are essential in studying the dynamics of such a system [1, 2]. The US Navy's concept for an all-electric ship has pushed forward the study of electromagnetic railguns, especially in the area of extending rail lifetime and thermal control of quick, successive launches [3]. To this point little is understood about the interaction between the armatures and rails. Large forces, currents, magnetic fields, and sliding contact surfaces create a unique dynamical problem, and those extreme conditions along with a bulky containment make sensors and experimental data collection hard to come by [4, 5]. Further comprehension of the dynamics of an electromagnetic railgun system is necessary to understand this rail and armature interaction in order to affect design changes and extend the rail lifetime.

As electromagnetic railguns are capable of launching projectiles at high velocities, there are many possibilities in regard to their range of uses. The most commonly thought of is as a weapon. High projectile speeds give the railgun long range and armor piercing capabilities that have not been seen before. Implementation into an all-electric battle ship would increase the ship's attack radius and penetration capabilities as well as decrease the weight and volume of ammunition carried aboard. Standard battleship rounds are currently propelled by an explosive, i.e. gun powder, and are not only bulky in size but also heavy in weight. Railguns would eliminate the need for that extra size and weight. Another possible use under investigation is micro-satellite launch. Putting a large communication satellite into orbit is expensive; on the other hand small micro-satellites could be launched into orbit relatively cheaply. Although, this requires launch speeds in excess of 10 km/s, well above typical railgun launch speeds [6]. While this is possible, the forces and dynamics of such a system become increasingly more complex. Damage to the micro-satellite under large pressures and magnetic fields during

launch would have to be strictly controlled in some manner in order to maintain the satellites working integrity. Even though most railgun research is focused on solid armatures, plasma armatures have their benefits too. Specifically, the high energy of plasma armature launches have been theoretically thought to be capable of impact fusion reaction [7]. The idea is to miniaturize the electromagnetic railgun concept and encircle a group of molecules with multiple railguns within a chamber. Filling the chamber with a controlled gas and firing upon the molecules from all directions would provide the energy needed to start the reaction through impact. This theory has been criticized though since scaling down to sizes that small has not been done before, and from a control standpoint, the exact timing of impact from multiple railguns would be extremely difficult to manage.

A railgun works from the simple physics of the interaction of current-induced magnetic fields. Figure 1.1 shows the principle of a railgun design with the armature velocity in the direction of the Lorenz force. The current flows through the rails, and a magnetic field is induced around the rails as shown in blue. When the current runs across the armature, an electromagnetic force is generated due to the current moving through the magnetic field. The Lorenz force can be calculated by Eq. (1.1) the cross product of current density vector (J) and the magnetic field vector around the rails (B), but the

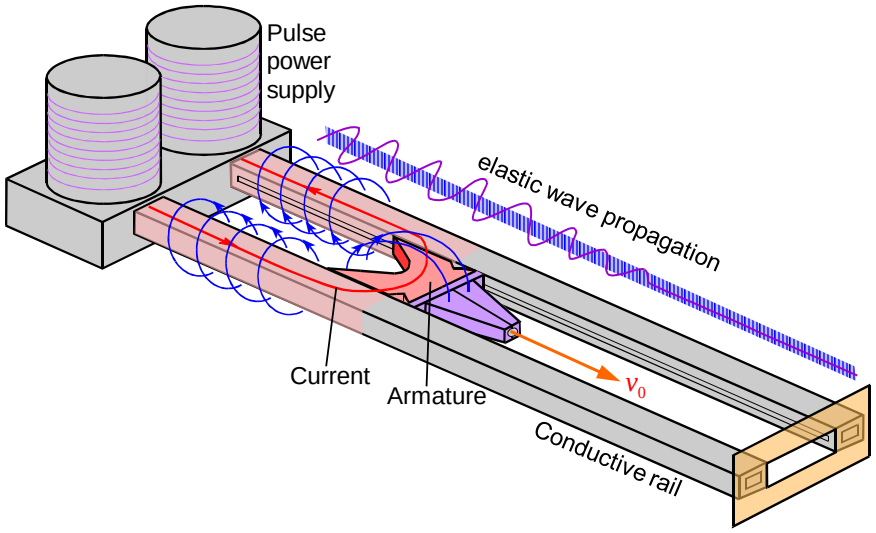

Figure 1.1: Railgun design and working principle.

magnetic field around the rails is proportionally induced by the current within the rails, so the Lorenz force is effectively proportional to the current density squared.

$$F_{Lorenz} = J \times B \tag{1.1}$$

Moreover, at the same time, the current across the armature is creating its own magnetic field and the current along the rails runs through this magnetic field. This creates Lorenz forces in the rails as well pushing them outward, transversely away from each other introducing the need for containment. Typical railguns produce extremely large Lorenz forces which cause launch accelerations ranging from 10^4 to 10^6 times gravity, launch velocities in the range of 1 to 3 km/s, contact pressures in the range of 10 to 500 MPa, current densities around 0.1 MA/cm^2, and peak currents in the range of 100 *kA* to 5 *MA* [5].

These extreme interfaces are pushing the limits of the present understanding of sliding electrical contact surfaces. Structural deformations and damages are severe and they limit the lifetime of the rails. To overcome this obstacle three main types of damage must be examined, understood, and acted upon [3]. Startup damage exists in the first third of the rail. This occurs when the very high current is transmitted through the same point of the rail for a relatively long time as the armature velocity is slow and it causes thermal damage and melting. For moderate velocity shots less than two kilometers per second there is armature transitioning. Armature transitioning is when the armature loses contact with the rails during launch [8-12]. For high velocity shots greater than two kilometers per second a failure mode called gouging exists [2, 13, 14]. The focus of this work is more related to modeling the rail and armature dynamics so start-up damage will be overlooked.

Armature transitioning exists in moderate velocity shots (< 2 km/s). When the armature moves along the rail, it causes deformation waves along the length of the rail. As it accelerates it begins to pass over those waves causing excitation of the elastic system. Vibrations such as these cause the armature to pitch, roll, and yaw. The resulting forces and intermittent contact between the rail and armature follow elastic behavior, bouncing away from each other effecting a loss of contact between them [9, 10].

Gouging is damage caused by material interaction between the rails and armature in the form of material removal or melting. Dynamic deformations of the rails due to the

extreme forces and conditions cause slight gaps between the armature and rails allowing the armature to pitch, yaw, and roll. These movements cause intermittent contact between the armature and rails. When inertial forces are so great that the materials exhibit fluid-like behavior, shock-induced pressure creates a region of plasticity under the location of impact [2]. Tangential motion of one body with respect to the other shears and deforms material at the points of impinging contact. When the shearing forces and interaction region becomes large enough to remove material, a gouge has been formed. Continual use and interaction will result in the gouge growing until the materials are no longer in contact [13].

Friction loss is a possible occurrence at high speeds. At a velocity of 3 km/s the friction loss is about 5% of the electrical loss, and significant increases up to 20% have been observed at 5 km/s [15]. The friction force strongly depends on the dynamic deformation characteristics of the rails because small deformations due to loading and stress waves can have a dramatic effect on the contact pressure and flow of current between the armature and rails [16, 17]. This has been experimentally shown around the critical speed using finite element analysis (FEA) [10, 11, 18]. Moreover, it is true even at the beginning of launch when the armature's speed is well below the critical speed, that small deformations radically affect the contact pressure and current flow [19].

1.2 Motivation

As armature transitioning and gouging are mainly caused by dynamic interaction between the armature and rails, study of structural dynamics should play a key role in understanding railgun dynamics and bore life. There are many studies on wave dynamics of rail-foundation systems, and many wave effects have been observed in experiments [1, 5, 10-12, 14-27]. However, phenomenological observations are the heart of almost all of these studies. Literature review indicates that the actual causes and physical implications of the three characteristic speeds known as critical, shear, and bar speeds are not clearly revealed and understood even up to this moment. For example, the critical speed is often described to be the minimum speed at which an unattenuated wave can radiate from the moving load - that is a phenomenological definition, but what causes the radiating wave is not fully known. The causes of shear and bar speeds are not well studied and

understood in the literature either because most conventional engineering applications only involve speeds that are well below the shear speed. For example, Achenbach and Sun [27] explained the shear and bar speeds to be the armature speeds when a leading or a trailing resonance occurs, but the formation and shape of the waveform are not looked at. Furthermore, Chen and Huang [23] explained the critical speed to be the speed when the rail-foundation resonance happens at $\omega = \sqrt{k/m}$, where k=spring constant of the insulator and m=mass per unit length of the rail. We show in this work that $\omega = \sqrt{k/m}$ corresponds to the bar speed, instead of the critical speed. For a rail-foundation system, a harmonic force at a fixed location can excite and radiate a transverse elastic wave away only if the excitation frequency is greater than a critical excitation frequency, but no relation is known between this critical excitation frequency and the critical speed [28]. Moreover, why and how do the waveforms change at the characteristic speeds is not understood along with the physical implications of different waveforms around these speeds. Most reports in the literature only examine the transverse deformation and bending rotation because Timoshenko's beam theory uses these two variables, but the role of shear rotation has not been studied.

Before now, studies on characteristic speeds and wave dynamics of rail-foundation systems have used multiple methods including complicated Fourier transforms. Huang proposed a unique dynamic stiffness method which is easier and more straightforward for derivation and understanding than the Fourier transform, but is inapplicable for our use as it only works for armature speeds below the shear speed [23, 24]. This paper proposes an alternative, generalized dynamic stiffness method for the study of wave dynamics of rail-foundation systems that will be valid and accurate for all speeds. The actual causes and physical implications of the three characteristic speeds will be investigated through detailed derivation, reasoning, and numerical simulations which show wave propagation dynamics as well as physical phenomena around and between characteristic speeds. Moreover, acoustics and optical modes will be used to show that high speed wave dynamics is primarily caused by interactions between bending and shear rotations.

CHAPTER 2

GOVERNING EQUATIONS

2.1 Electromechanical Model

In this work railguns will be modeled as a beam on an elastic foundation. The rails are usually made of copper alloys, and separated from a rigid outside containment (laminated steel) by an insulator. An elastic foundation is used to account for the elastic behavior of the rail insulator which is often made of a fiberglass material called G-10 or garolite (similar to the circuit board material FR-4). A simple electromechanical model of the system is shown in Fig. 2.1. A capacitor bank is used as the power source, and the changing rail length in which the current flows is modeled as a variable inductor.

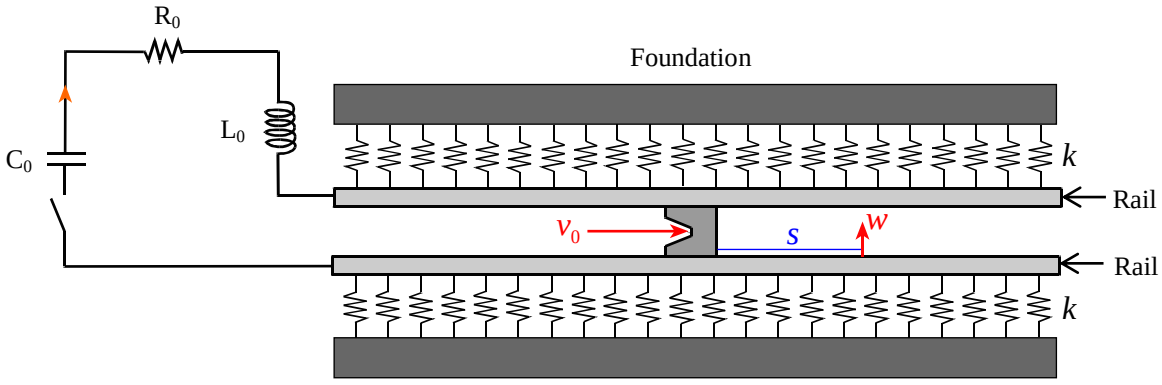

Figure 2.1: Electromechanical model of a railgun with a capacitor power supply.

2.2 Electrical model

The fundamental equations of motion for a capacitor driven electromagnetic launcher can be derived using an electromechanical Lagrangian L. Fig. 2.1 shows the electromechanical model of launcher where the circuit consists of a capacitor with a capacitance C_0, an inductor with an inductance L_0, and an overall resistance R_0. The barrel, treated as a variable inductor, can be modeled as a linear function of the armature position which agrees well with experiments. Therefore, we assume

$$L(x) = L'u, \quad L' = \text{constant} \tag{2.1}$$

where u is the armature's displacement, $\dot{u} \equiv du/dt = v_0$, and L' is referred to as the inductance gradient of the launcher. For an infinite pair of rectangular conductors running parallel to one another, we have [18]

$$L' = \frac{\mu_0}{\pi}\left(\log\left(\frac{d}{B+C}\right) + 1.5 + \Delta_k - \Delta_e\right) \tag{2.2}$$

where d is the distance between the centers of rails, and B and C represent their cross-sectional dimensions with C bring the smaller one. Variables Δ_k and Δ_e are tabulated in Grover's book [29]. For example, the Cornell launcher has Δ_k=0.389 and $\Delta_e = 0.00249$, and hence we obtain $L' = 0.273\ \mu H/m$ from Eq. (2.2), which is only an approximation because the rail length is finite here. An experimental value of L'can be found using a precision LCR meter.

The electromechanical Lagrangian L of the system is given by

$$L = \frac{1}{2}m\dot{u}^2 - \frac{1}{2C_0}q^2 + \frac{1}{2}(L_0 + L'u)\dot{q}^2 \tag{2.3}$$

The loss of armature mass during launching is neglected. The Rayleigh dissipation function $\Re$ is defined as

$$\Re = \mu N\dot{u}\,\mathrm{sgn}(\dot{u}) + \frac{1}{2}R_0\dot{q}^2 \tag{2.4}$$

where N is the normal contacting force, q is the charge, and μ is the friction coefficient. Hence, we obtain from Lagrange's equation that

$$\frac{d}{dt}\left(\frac{\partial L}{\partial \dot{u}}\right) - \frac{\partial L}{\partial u} + \frac{\partial \Re}{\partial \dot{u}} = 0 \Rightarrow m\ddot{u} + \mu N\,\mathrm{sgn}(\dot{u}) = \frac{1}{2}L'\dot{q}^2 \tag{2.5}$$

$$\frac{d}{dt}\left(\frac{\partial L}{\partial \dot{q}}\right) - \frac{\partial L}{\partial q} + \frac{\partial \Re}{\partial \dot{q}} = 0 \Rightarrow (L_0 + L'u)\ddot{q} + (R_0 + L'\dot{u})\dot{q} + \frac{1}{C_0}q = 0 \tag{2.6}$$

where the initial condition is $q(0) = q_0$. These are two coupled nonlinear ordinary differential equations. Eq. (2.5) clearly shows that the propulsion force on the launcher is

$$P_{prop} = \frac{1}{2}L'\dot{q}^2 \tag{2.7}$$

This simple approximation works surprisingly well when compared to experimental data [18].

2.3 Bernoulli-Euler Beam Model

Little research has been done on the dynamics of railguns, but some modeling has been done using Bernoulli-Euler and Timoshenko beam models. For the general beam shown in Fig. 2.2, if it is assumed to be a Bernoulli-Euler beam, Fig. 2.3 shows the loads on the free-body diagram of a differential element.

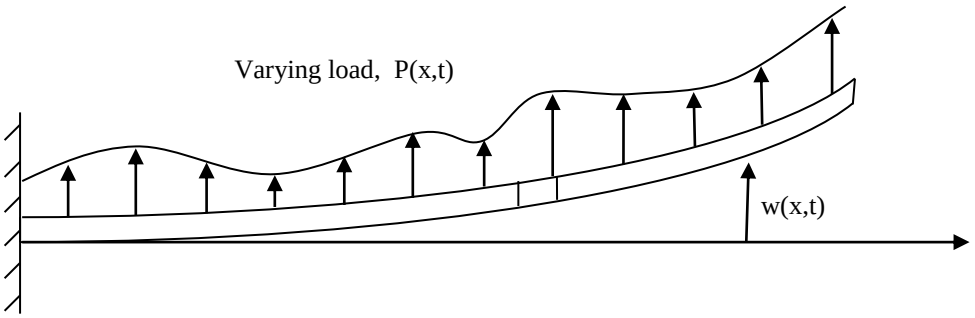

Figure 2.2: A cantilevered beam subject to a general distributed load.

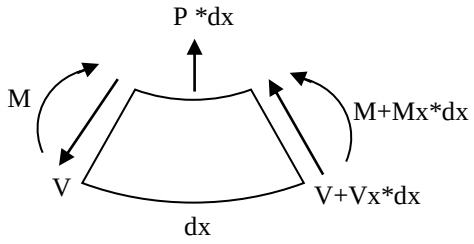

Figure 2.3: A differential element of a Bernoulli-Euler beam.

From the free-body diagram, Eq. (2.8) is derived to be the equation of motion where w(x,t) is the displacement of the rail, $w' \equiv \partial w / \partial x = \theta$, and $\dot{w} \equiv \partial w / \partial t$. Taking Fig. 2.2 as our base model then adding an insulator and a rigid foundation underneath effectively introduces a spring force and a damper force in beneath the free-body diagram in Fig. 2.3. From this we get Eq. (2.9). As the containment is multiple orders of magnitude more rigid than the rail and insulator, modeling it as a rigid body will not adversely affect the accuracy of our model. Furthermore applying a pretension loading on the rails can have positive effects on the dynamics of the system. Adding a pretension loading N causes a longitudinal force in the free body diagram and directly affects the shear forces. Through some derivations with the inclusion of a longitudinal force we obtain Eq. (2.10) [30, 31].

$$m\ddot{w} + (EIw'')'' - (J\ddot{w}')' = P \tag{2.8}$$

$$m\ddot{w} + c\dot{w} + kw + (EIw'')'' - (J\ddot{w}')' = P \tag{2.9}$$

$$m\ddot{w} + c\dot{w} + kw + Nw'' + (EIw'')'' - (J\ddot{w}')' = P \tag{2.10}$$

For Eq. (2.8)-(2.10), m is the mass of the rail per unit length, c is the damping coefficient of the insulator per unit length, k is the stiffness of the insulator per unit length, E is Young's modulus of the rail, I is the area moment of inertia of the rail, J is the rotary inertia of the rail per unit length, and f(x,t) is the distributed load per unit length. For a uniform isotropic beam, m = Aρ and J = Iρ, where ρ is the density of the beam material. We add the term Nw'' to account for any possible longitudinal compressive pre-load in order to understand the influences of preloading on characteristic speeds. This type of model only works for systems under low frequency excitations because the Bernoulli-Euler model predicts that waves can travel at a high frequency with a speed of infinity, which is erroneous [28].

2.4 Timoshenko Beam Model

A Timoshenko model takes into account two deformation variables, w and ψ, pictured in Fig. 2.4. The governing equations are derived using Newton's second law and are shown in Eqs. (2.11) and (2.12), where Eq. (2.11) governs the transverse vibration, and Eq. (2.12) governs the rotational vibration [31].

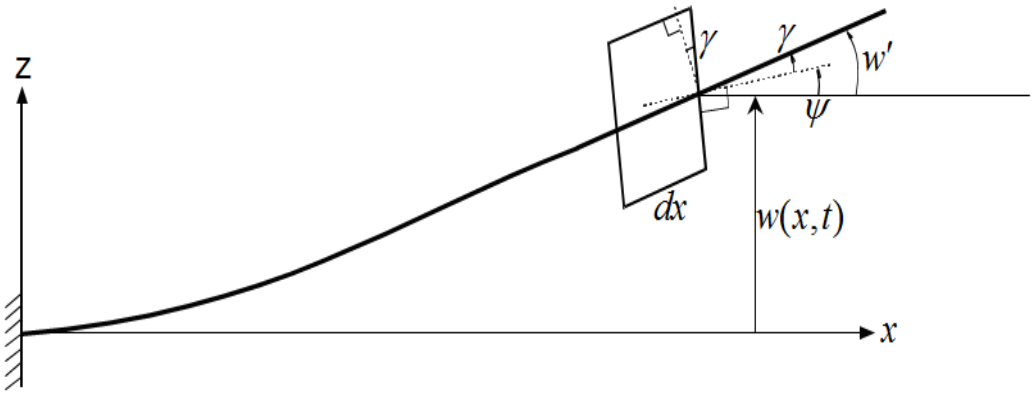

Figure 2.4: Timoshenko beam model and variables.

$$m\ddot{w} + c_1\dot{w} + kw + Nw'' + \left(kAG\left(\psi - w'\right)\right)' = P \tag{2.11}$$

$$J\ddot{\psi} + c_2\dot{\psi} - (EI\psi')' - kAG(w' - \psi) = 0 \tag{2.12}$$

where $\psi(= w' - \gamma)$ is the bending rotation angle of the deformed cross section, γ is the shear rotation angle of the cross section, c_1 and c_2 are the corresponding material damping coefficients per unit length of the beam, and κ is the shear correction factor. For isotropic beams with rectangular cross-sections, $\kappa = 5/6$ [31, 32, 33]. The G-10 material for the rail insulator is actually a viscoelastic material, and Eq. (2.11) shows that the c_1 can also be used to account for the damping property of G-10.

For a uniform beam, one can substitute ψ' from Eq. (2.11) into $\partial[Eq.(2.12)]/\partial x$ to obtain the following high-order equation:

$$\begin{aligned} &EI\left(1-\frac{N}{\kappa AG}\right)w^{iv} + \left(N - \frac{EIk}{\kappa AG}\right)w'' - \left(\left(1-\frac{N}{\kappa AG}\right)J + \frac{mEI}{\kappa AG}\right)\ddot{w}'' - \left(\left(1-\frac{N}{\kappa AG}\right)c_2 + \frac{c_1 EI}{\kappa AG}\right)\dot{w}'' \\ &+ \left(c_1 + \frac{kc_2}{\kappa AG}\right)\dot{w} + \left(m + \frac{Jk + c_1c_2}{\kappa AG}\right)\ddot{w} + \left(\frac{c_1J + c_2m}{\kappa AG}\right)\dddot{w} + \frac{Jm}{\kappa AG}\ddddot{w} + kw \\ &= P - \frac{EI}{\kappa AG}P'' + \frac{c_2}{\kappa AG}\dot{P} + \frac{J}{\kappa AG}\ddot{P} \end{aligned} \tag{2.13}$$

Some of the terms in Eq. (2.13) are not accounted for in the literature (e.g., [9,10,22,23]). To neglect shear deformation one can substitute $G \to \infty$, $c_1 = c$ and $c_2 = 0$ into Eq. (2.13) to obtain the Bernoulli-Euler beam theory in Eq. (2.10).

CHAPTER 3

CHARACTERISTIC SPEEDS

3.1 Shear and Bar Speeds

Under free or boundary-excited vibrations (i.e., *P=0*), solutions of Eq. (2.13) have the form

$$w = \mathrm{e}^{\mathrm{j}(\beta x - \omega t)},\ \beta = \frac{2\pi}{\lambda} \tag{3.1}$$

where ω is the vibration frequency, β is the wave number, $\mathrm{j} \equiv \sqrt{-1}$, and λ is the wavelength. Substituting Eq. (3.1) into Eq. (2.13) with $P = 0$ yields

$$EI\left(1-\frac{N}{\kappa AG}\right)\beta^4 - \left(N - \frac{EIk}{\kappa AG}\right)\beta^2 - \left(\left(1-\frac{N}{\kappa AG}\right)J + \frac{mEI}{\kappa AG}\right)\beta^2\omega^2 - \mathrm{j}\left(\left(1-\frac{N}{\kappa AG}\right)c_2 + \frac{c_1 EI}{\kappa AG}\right)\beta^2\omega$$
$$-\mathrm{j}\left(c_1 + \frac{kc_2}{\kappa AG}\right)\omega - \left(m + \frac{Jk + c_1c_2}{\kappa AG}\right)\omega^2 + \mathrm{j}\left(\frac{c_1 J + c_2 m}{\kappa AG}\right)\omega^3 + \frac{Jm}{\kappa AG}\omega^4 + k = 0 \tag{3.2}$$

If $P = N = c_1 = c_2 = 0$, i.e. neglecting damping and pre-compression, Eq. (3.2) reduces to

$$EI\beta^4 + \frac{EIk}{\kappa AG}\beta^2 - \left(J + \frac{mEI}{\kappa AG}\right)\beta^2\omega^2 - \left(m + \frac{Jk}{\kappa AG}\right)\omega^2 + \frac{Jm}{\kappa AG}\omega^4 + k = 0 \tag{3.3}$$

This dispersion equation relates ω to β, and it can be used to calculate the phase and group velocities of an elastic wave. The phase velocity v_p is the propagating speed of a harmonic wave. If a constant-phase point of a harmonic waveform is followed, we have $\beta x - \omega t = \text{const.}$ and

$$v_\mathrm{p} = \frac{\mathrm{d}x}{\mathrm{d}t} = \frac{\omega}{\beta} \tag{3.4}$$

The group velocity v_g is the propagating speed of a multi-harmonic wave's modulated amplitude [28], and it is the speed at which a multi-harmonic wave's energy and information travel in a medium and is given by

$$v_g = \frac{d\omega}{d\beta} \tag{3.5}$$

Because v_p should be a finite number for any elastic wave in a beam [28], we have $\beta\ (=2\pi/\lambda) \to \infty$ when $\omega \to \infty$. Hence, it follows from Eq. (3.3) that

$$\frac{Jm}{\kappa AG}\omega^4 - \left(J + \frac{mEI}{\kappa AG}\right)\omega^2\beta^2 + EI\beta^4 = 0 \Rightarrow \omega = \pm\beta\sqrt{\frac{\kappa G}{\rho}}, \pm\beta\sqrt{\frac{E}{\rho}} \tag{3.6}$$

For a wave with $\omega < 0$, Eqs. (3.1) and (3.4) indicate that it is nothing but a wave propagating along the *–x* direction. So, Eqs. (3.4) and (3.6) define two characteristic phase speeds [33, 34]:

$$V_{\text{shear}} \equiv \sqrt{\frac{\kappa G}{\rho}}, \quad V_{\text{bar}} \equiv \sqrt{\frac{E}{\rho}} \tag{3.7}$$

Next we explain the physical implications of these two characteristic speeds. With $\omega \to \infty, \beta \to \infty$ and $P = N = c_1 = c_2 = 0$, Eqs. (2.11) and (2.12) reduce to

$$m\ddot{w} - \kappa AGw'' = 0 \tag{3.8}$$

$$J\ddot{\psi} - EI\psi'' = 0 \tag{3.9}$$

At high frequencies, Eq. (3.8) shows that the transverse displacement *w* is caused by vertical shearing ($\because \psi = 0$ and $w' = \gamma$), as shown in Fig. 3.1. Eq. (3.9) shows that the cross-sectional rotation ψ is caused by horizontal shearing ($\because w' = 0$ and $\psi = -\gamma$) and it results in repeated compression/extension on upper/lower parts of the cross section, as shown in Fig. 3.2. Substituting Eq. (3.1) and $\psi = e^{j(\beta x - \omega t)}$ into Eqs. (3.8) and (3.9) yields Eq. (3.7). Hence, Eqs. (3.7)-(3.9) reveal that these two speeds are the propagating speeds of a transverse shear wave and a horizontal shear wave, respectively. Eq. (3.8) behaves like a string under a pretension $\tau = \kappa AG$ [31], and thus the wave speed at any frequency is $\sqrt{\tau/m} = \sqrt{\kappa G/\rho}$. As $w' = 0$ in Eq. (3.9), the beam behaves like a rigid bar on an elastic foundation (see Fig. 3.2). Hence, the bar speed V_{bar} corresponds to resonance at $\omega = \sqrt{k/m}$. Substituting $\omega = \sqrt{k/m}$ into Eq. (3.3) yields $\beta = \sqrt{kJ/EIm} = \sqrt{k\rho/Em}$ and therefore $\omega/\beta = \sqrt{E/\rho} = V_{\text{bar}}$, which is the speed of any longitudinal

extension/compression wave in the material. For isotropic materials, $V_{\text{shear}} < V_{\text{bar}}$ because $\kappa G = \kappa E/(2+2\nu) < E$, where ν is the Poisson ratio. Since a wave propagating at V_{bar} has no relative transverse deflection $(\because w' = 0)$, V_{shear} is the highest speed for any transverse deflection waves. Figs. 3.1 and 3.2 show that shear and bar speeds can be realized only if the shear rotation γ is included in the modeling.

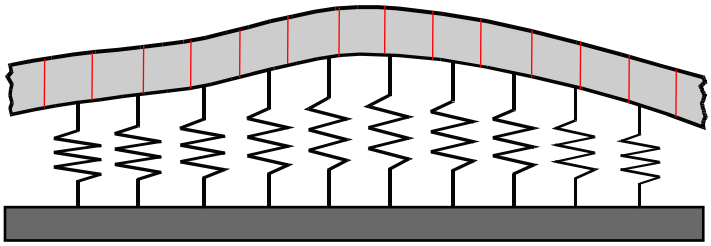

Figure 3.1: Rail deformation pattern at the shear speed (transverse shear wave).

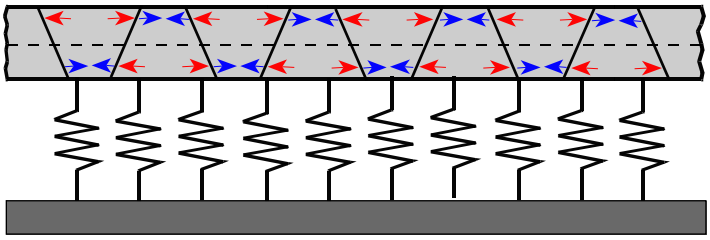

Figure 3.2: Rail deformation pattern at the bar speed (longitudinal shear wave).

When ω is given a value, the wave numbers from Eq. (3.3) are of the following form.

$$\beta^2 = \frac{-\hat{r}_2 \pm \sqrt{\hat{R}}}{2\hat{r}_1},\ \hat{R} \equiv \hat{r}_2^2 - 4\hat{r}_1\hat{r}_3$$

$$\hat{r}_1 \equiv EI, \hat{r}_2 \equiv \frac{EIk}{\kappa AG} - \left(J + \frac{mEI}{\kappa AG}\right)\omega^2, \hat{r}_3 \equiv -\left(m + \frac{Jk}{\kappa AG}\right)\omega^2 + \frac{Jm}{\kappa AG}\omega^4 + k \qquad (3.10)$$

$$\text{If } \hat{R} < 0: \beta_{\text{i}} = (\hat{a} \pm \text{j}\hat{b}, -\hat{a} \pm \text{j}\hat{b}), \hat{a} > 0, \hat{b} > 0$$

$$\text{If } \hat{R} > 0: \beta_{\text{i}} = (\pm\hat{a}_1, \pm\hat{a}_2), (\pm\text{j}\hat{b}_1, \pm\text{j}\hat{b}_2), \text{or } (\pm\hat{a}_1, \pm\text{j}\hat{b}_2), \hat{a}_{\text{i}} > 0, \hat{b}_{\text{i}} > 0$$

For $\hat{R} < 0$, Eqs. (3.10) and (3.1) show that $\hat{a} + \text{j}\hat{b}$ and $-\hat{a} - \text{j}\hat{b}$ represent two exponentially decaying waves moving to the right and left, respectively. Moreover, $\hat{a} - \text{j}\hat{b}$ and $-\hat{a} + \text{j}\hat{b}$ are impossible solutions because they grow to infinity at far sites. For $\hat{R} > 0$, $\text{j}\hat{b}_2$ and $-\text{j}\hat{b}_1$ are exponentially decaying solutions, and $-\text{j}\hat{b}_2$ and $\text{j}\hat{b}_1$ are impossible

exponentially growing solutions moving to the right and left, respectively. However, $\hat{a}_1$ and $\hat{a}_2$ represent two possible non-decaying waves propagating to the right, and $-\hat{a}_1$ and $-\hat{a}_2$ represent two possible non-decaying waves propagating to the left. Hence, $\hat{R}=0$ determines the critical (cut-on) frequency that can excite the beam to have a propagating wave, and the corresponding critical speed ($=\omega/\beta=\omega/\hat{a}$) is the minimum phase velocity for a harmonic wave to propagate away [34]. When $\hat{R}=0$, $\hat{a}_1=\hat{a}_2$. When $\hat{R}>0$, $\hat{a}_1$ and $\hat{a}_2$ are different due to different relative motions between w' and ψ (or γ). The high-speed mode is often called the optical mode, and the low-speed one is called the acoustic mode. The low-speed mode is often the main concern. For railguns, however, both speeds need to be examined because railguns may accelerate up to Mach 10 during launch [3].

However, this critical speed is under a harmonic excitation at a fixed location. For a railgun, its moving armature excites the system through dynamic interaction with dynamically deformed rails, and the corresponding critical speed is different, as shown in Section 3.2 below.

3.2 Critical Speed

In the derivation of the critical speed, V_c, of a rail-foundation system we consider Timoshenko's model in Eq. (2.13) with a concentrated load $\hat{P}$ moving at a constant velocity v_o along the x direction. After the load is applied for a while and damping exists, the beam deformation becomes a static geometry with respect to an observer traveling with the load. This is known as a quasi-stationary state. The dynamic stiffness method that Chen and Huang [23] presented is only good for waves at speeds below the shear speed. Hence we propose a generalized dynamic stiffness method that is applicable for waves at any speed and can deal with higher-order shear-deformable beam theories using two or more variables. In addition, we use the concepts of buckling and resonance to explain the physical implications of the critical speed and reveal different characteristic waveforms around the three characteristic speeds.

First, we define a moving spatial coordinate and derive the spatial and time derivatives of the transverse displacement as [1, 22-23, 27]

$$s \equiv x - v_0 t \Rightarrow w(x,t) = w(s,t),\ w' = \frac{\partial w}{\partial x}\Big|^{t=\text{const.}} = \frac{\partial w}{\partial s}\Big|^{t=\text{const.}}$$
$$\dot{w} = \frac{\partial w}{\partial t}\Big|^{x=\text{const.}} = \frac{\partial w}{\partial t}\Big|^{s=\text{const.}} - v_0 \frac{\partial w}{\partial s},\ \ \ddot{\dot{w}} = \left(\frac{\partial}{\partial t} - v_0 \frac{\partial}{\partial s}\right)^4 w \tag{3.11}$$

When the beam deformation becomes quasi-stationary we have

$$\frac{\partial w}{\partial t}\Big|^{s=\text{const.}} = 0 \tag{3.12}$$

and the solution has the following form:

$$w(s) = \mathrm{e}^{\alpha s} \tag{3.13}$$

As it is a concentrated load $\hat{P}$ at $s = x - v_0 t = 0$, we have $P(x,t) = \hat{P}\delta(s)$, where $\delta(s)$ is an impulse function known as the Dirac delta function. Substituting Eqs. (3.11)-(3.13) into Eq. (2.13) yields

$$\begin{aligned}
&(EI - Jv_0^2)\left(1 - \frac{N + mv_0^2}{\kappa AG}\right)\alpha^4 + \left(v_0 c_2 + \frac{(EI - Jv_0^2)c_1 v_0 - (N + mv_0^2)c_2 v_0}{\kappa AG}\right)\alpha^3 \\
&\quad + \left(N + mv_0^2 + \frac{c_1 c_2 v_0^2 - (EI - Jv_0^2)k}{\kappa AG}\right)\alpha^2 - \left(c_1 + \frac{k c_2}{\kappa AG}\right)v_0 \alpha + k \\
&= \left(\delta - \frac{c_2 v_0}{\kappa AG}\delta' - \frac{EI - Jv_0^2}{\kappa AG}\delta''\right)\hat{P}\mathrm{e}^{-\alpha s}
\end{aligned} \tag{3.14}$$

The terms $N + mv_0^2$ and $EI - Jv_0^2$ in Eq. (3.14) show how the armature's moving velocity affects the system's properties and hence changes the critical speed. Since the singular terms in Eq. (3.14) are zero (i.e., $P(x,t) = 0$) for the two separated domains $s > 0$ and $s < 0$, we will solve for solutions for these two separated domains. As all the coefficients in Eq. (3.14) are real numbers, the four wave numbers from Eq. (3.14) with *P=0* are in the following form:

$$\alpha_{\mathrm{i}} = (a_1 + \mathrm{j}b_1, a_2 + \mathrm{j}b_2, a_1 - \mathrm{j}b_1, a_2 - \mathrm{j}b_2),\ \ a_1 \geq 0, b_1 \,\&\, b_2 \geq 0 \tag{3.15}$$

where a_{i} and b_{i} are real numbers and a_2 can be negative or positive. It follows from Eq. (3.15) that

$$\begin{aligned}
0 &= (\alpha - \alpha_1)(\alpha - \alpha_2)(\alpha - \alpha_3)(\alpha - \alpha_4) \\
&= \alpha^4 - 2(a_1 + a_2)\alpha^3 + (a_1^2 + a_2^2 + b_1^2 + b_2^2 + 4a_1 a_2)\alpha^2 \\
&\quad - 2(a_1 a_2^2 + a_1^2 a_2 + b_1^2 a_2 + a_1 b_2^2)\alpha + (a_1^2 + b_1^2)(a_2^2 + b_2^2)
\end{aligned} \tag{3.16}$$

Comparing Eqs. (3.14) and (3.16) we obtain

$$-2(a_1 + a_2) = \frac{c_1 v_0}{\kappa AG - N - m v_0^2} + \frac{c_2 v_0}{EI - J v_0^2} \tag{3.17}$$

Then from Eqs. (3.13) and (3.15) the quasi-stationary solution for $s > 0$ and $s < 0$ should be in the following form:

$$w(s) = \sum_{i=1}^{4} C_i e^{\alpha_i s} = C_1 e^{(a_1 + jb_1)s} + C_2 e^{(a_2 + jb_2)s} + C_3 e^{(a_1 - jb_1)s} + C_4 e^{(a_2 - jb_2)s} \tag{3.18}$$

Using Eqs. (3.11) and (3.12) and substituting Eq. (3.18) into Eq. (2.12) yields

$$\psi(s) = \sum_{i=1}^{4} D_i e^{\alpha_i s}, \;\; D_i = g_i C_i, \;\; g_i \equiv \frac{\kappa AG \alpha_i}{\kappa AG + (J v_0^2 - EI)\alpha_i^2 - v_0 c_2 \alpha_i} \tag{3.19}$$

If $N = c_2 = 0$, Eq. (3.17) indicates that $a_1 + a_2 < 0$ if $v_0 < \sqrt{\kappa G / \rho}$ $\left(= V_{\text{shear}}\right)$. If $a_1 > 0$ and $a_2 < 0$, it follows from Eqs. (3.13) and (3.18) that $e^{a_1 s}\big|^{s \to -\infty} \approx 0$, $e^{a_1 s}\big|^{s \to \infty} \to \infty$, $e^{a_2 s}\big|^{s \to -\infty} \to \infty$, and $e^{a_2 s}\big|^{s \to \infty} \approx 0$. Because it is an infinite beam, the solution should satisfy $w(\infty) = w(-\infty) = 0$ if any damping exists. Therefore, if $a_1 > 0$ and $a_2 < 0$, the quasi-stationary solution should be in the following form:

$$\begin{cases} w(s) = C_1 e^{(a_1 + jb_1)s} + C_3 e^{(a_1 - jb_1)s} & \text{for } -\infty < s < 0 \\ w(s) = C_2 e^{(a_2 + jb_2)s} + C_4 e^{(a_2 - jb_2)s} & \text{for } 0 < s < \infty \end{cases} \tag{3.20}$$

Because $w(s)$ should be a real function, C_1 and C_3 along with C_2 and C_4 should be complex conjugate to each other. Moreover, b_1 is the wave number, and $\lambda_1 = 2\pi / b_1$ is the wavelength of the wave within $-\infty < s < 0$. Alternately, b_2 is the wave number and $\lambda_2 = 2\pi / b_2$ is the wavelength of the wave within $0 < s < \infty$. At the point $s=0$, $w(s)$ and $\psi(s)$ should be continuous and the external concentrated force F and moment M should balance with the internal shear forces and moments. Therefore from the boundary conditions, we have

$$\begin{aligned} & w(0^-) = w(0^+), \;\; \psi(0^-) = \psi(0^+) \\ & F = V(0^-) - V(0^+) = \kappa AG\left(w_s(0^-) - \psi(0^-) - w_s(0^+) + \psi(0^+)\right) \\ & M = M(0^-) - M(0^+) = EI\left(\psi_s(0^-) - \psi_s(0^+)\right) \end{aligned} \tag{3.21}$$

where $w_s \equiv \partial w / \partial s$, $\psi_s \equiv \partial \psi / \partial s$, $V(0^-)$ and $V(0^+)$ are internal shear forces, and $M(0^-)$ and $M(0^+)$ are internal bending moments. Substituting Eqs. (3.20) and (3.19) into Eq. (3.21) gives

The $[K]$ matrix here is called a generalized dynamic stiffness matrix, and it is a function of the moving load speed v_0.

When $|[K]| = 0$ occurs for a specific value of v_0, the displacement variables C_{i} $(\mathrm{i} = 1 \sim 4)$ cannot be obtained from Eq. (3.22) and the actual deformed geometry is unknown. In other words, the buckling load of the beam-foundation system becomes zero, and a small transverse load can cause huge displacement in the rails, meaning the system stability margin has been reached. It also means that a harmonic excitation force with a frequency close to zero can cause resonance. Hence, $|[K]| = 0$ determines the critical velocity (i.e., $v_0 = V_{\mathrm{c}}$).

If no damping, $c_1 = c_2 = 0$, the coefficients of α^3 and α in Eq. (3.14) are zero and we obtain

$$\alpha^2 = \frac{\dfrac{EIk}{\kappa AG} - N - \left(m + \dfrac{Jk}{\kappa AG}\right)v_0^2 \pm \sqrt{R}}{2(EI - Jv_0^2)\left(\kappa AG - N - mv_0^2\right)/\kappa AG}$$
$$R \equiv \left(\frac{EIk}{\kappa AG} + N + \left(m - \frac{Jk}{\kappa AG}\right)v_0^2\right)^2 + 4k(Jv_0^2 - EI) \tag{3.23}$$

If $R = 0^- < 0$, we obtain from Eqs. (3.23), (3.15), (3.19) and (3.22) that

$$\alpha_{\mathrm{i}} = (a_1 + \mathrm{j}b_1, a_2 + \mathrm{j}b_2, a_1 - \mathrm{j}b_1, a_2 - \mathrm{j}b_2)$$
$$a_2 = -a_1 < 0, b_2 = b_1 > 0, \alpha_4 = -\alpha_1,\ \alpha_3 = -\alpha_2, g_4 = -g_1, g_3 = -g_2$$
$$|[K]| = 4\kappa AGEI(\alpha_1 g_2 - \alpha_2 g_1)(\alpha_2 g_2 - \alpha_1 g_1) \tag{3.24}$$

Contrarily, if $R = 0^+ > 0$ and $\alpha^2 < 0$, we obtain from Eqs. (3.23), (3.15), (3.19) and (3.22) that

$$\alpha_i = (\mathrm{j}b_1, \mathrm{j}b_2, -\mathrm{j}b_1, -\mathrm{j}b_2),\ a_1 = a_2 = 0, 0 < b_1 < b_2$$
$$\Rightarrow \alpha_3 = -\alpha_1, \alpha_4 = -\alpha_2, g_3 = -g_1, g_4 = -g_2$$
$$|[K]| = -4\kappa AGEI(\alpha_1 g_2 - \alpha_2 g_1)(\alpha_2 g_2 - \alpha_1 g_1) \tag{3.25}$$

Finally, if $R = 0$, we have $\alpha_2 = \alpha_1$ and $g_2 = g_1$ and hence $|[K]| = 0$ for Eq. (3.24) and Eqs. (3.25). This argument is similar to that for Eq. (3.10). That is why the critical speed corresponds to $R = 0$ and it follows from Eq. (3.23) that, if no damping,

$$V_c = \pm\sqrt{\frac{-r_2 + \sqrt{r_2^2 - 4r_1 r_3}}{2r_1}}$$
$$r_1 \equiv \left(m - \frac{Jk}{\kappa AG}\right)^2, r_2 \equiv 2\left(m - \frac{Jk}{\kappa AG}\right)\left(\frac{EIk}{\kappa AG} + N\right) + 4kJ, r_3 \equiv \left(\frac{EIk}{\kappa AG} + N\right)^2 - 4kEI \tag{3.26}$$

where $V_c < 0$ is for the case with $v_0 < 0$. Moreover, if N = c_2 = 0 but $c_1 \neq 0$, Eq. (3.17) indicates that $0 < a_1 < -a_2$ (or $a_1 + a_2 < 0$) if $v_0 < V_{shear}$. Hence, the waveforms on the two sides of the load are different. Substituting $v_0 = V_{bar} = \sqrt{E/\rho}$ into the R in Eq. (3.23) yields $R = (N + EA)^2$. In other words, $V_c < V_{bar}$ and $V_c = V_{bar}$ only if a pre-compression force $N = -EA$ is applied on the beam to make $R=0$. However, this is physically impossible because a pretension force of EA means that the beam needs to be stretched to have a strain value of one. Since V_c is determined by the buckling phenomenon, pretension increases the buckling load and therefore the critical speed as well. Next we explain the cause and physical implication of the critical speed V_c. When $v_0 = V_c$, $a_1 = a_2 = 0$ and $b_1 = b_2$. Hence, it is a standing harmonic wave (consisting of two harmonic waves having the same amplitude and frequency but traveling along opposite directions) with a wavelength $\lambda = 2\pi / b_1$. Substituting $\beta = b_1$ and $\omega = b_1 v_0$ (i.e. $v_0 = \omega / \beta$) into Eq. (3.3) yields 0=0. In other words, when the wave oscillates for one period, the load moves across exactly one wavelength of the standing wave. This synchronous motion causes resonance and thus divergence. The quasi-stationary buckling strength of the beam-foundation system then becomes zero. Civil engineers use the same concept to define the

critical speed for a car on a bridge by using the bridge length as $\lambda/2$ $(=\pi/\beta)$ and the first standing-mode frequency as the vibration frequency [36].

For Bernoulli-Euler beams, substituting $J=0$ and $G\to\infty$ into Eq. (3.26) yields

$$V_{\mathrm{c}}=\pm\sqrt{\frac{\sqrt{4kEI}-N}{m}} \tag{3.27}$$

For the reason that V_c is determined by $E^{1/4}$, it is difficult to increase V_c by increasing *E*. Eq. (3.27) also clearly indicates that a tension loading (N<0) increases the value of V_{c}.

3.3 Quasi-Stationary Waveforms

To obtain the quasi-stationary waveform for a concentrated load traveling along an infinite beam on an elastic foundation, one needs to assume a loading value (e.g., $F=\hat{F}$), solve for C_{i} $(\mathrm{i}=1\sim4)$ using Eq. (3.22), and then use Eqs. (3.18) and (3.19) to obtain $w(s)$ and $\psi(s)$. However, Eqs. (3.20) and (3.22) are only valid for $v_0<V_{\mathrm{shear}}$.

When v_0 changes from $v_0<V_{\mathrm{shear}}$ to $v_0>V_{\mathrm{shear}}$, the term $(\kappa AG-N-mv_0^2)$ in Eq. (3.23) changes sign (if $N=0$) and thus we have

$$\text{if } V_{\mathrm{shear}}<v_0<V_{\mathrm{bar}}:\alpha_{\mathrm{i}}=\left(\mathrm{j}b_1,a_2,-\mathrm{j}b_1,-a_2\right),a_1=b_2=0,a_2<0 \tag{3.28}$$

Hence, the term $C_4\mathrm{e}^{\alpha_4 s}$ with $\alpha_4=-a_2$ should be excluded from the solution for $s>0$ and included in the solution for $s<0$, i.e.,

$$\begin{cases} w(s)=C_1\mathrm{e}^{\alpha_1 s}+C_3\mathrm{e}^{\alpha_3 s}+C_4\mathrm{e}^{\alpha_4 s} & \text{for } -\infty<s<0 \\ w(s)=C_2\mathrm{e}^{\alpha_2 s} & \text{for } 0<s<\infty \end{cases} \tag{3.29}$$

Substituting Eq. (3.29) into Eq. (3.21) yields Eq. (3.22) with the negative signs in the fourth column of $[K]$ being removed.

When v_0 changes from $v_0<V_{\mathrm{bar}}$ to $v_0>V_{\mathrm{bar}}$, the term $(EI-Jv_0^2)$ in Eq. (3.23) changes sign and we have

$$\text{if } V_{\mathrm{bar}}<v_0:\alpha_{\mathrm{i}}=\left(\mathrm{j}b_1,\mathrm{j}b_2,-\mathrm{j}b_1,-\mathrm{j}b_2\right),a_1=a_2=0 \tag{3.30}$$

If any damping exists (i.e., c_1 and/or $c_2 > 0$), both a_1 and a_2 are positive. Hence, the solution has the following form:

$$\begin{cases} w(s) = C_1 e^{\alpha_1 s} + C_2 e^{\alpha_2 s} + C_3 e^{\alpha_3 s} + C_4 e^{\alpha_4 s} & \text{for } -\infty < s < 0 \\ w(s) = 0 & \text{for } 0 < s < \infty \end{cases} \tag{3.31}$$

In other words, $w(s) = \psi(s) = 0$ for $s>0$. There are no waves in front of the moving load because V_{bar} is the highest possible speed for any elastic waves to propagate in an elastic medium. However, there are waves right behind the moving load even when the load moves at a speed higher than V_{bar}, because a moving load can drag a deformed wave pattern faster than V_{bar}. Substituting Eq. (3.31) into Eq. (3.21) with $w(0^+) = \psi(0^+) = 0$ yields Eq. (3.22) with the negative signs in the second and fourth columns of $[K]$ being removed. When $v_0 = V_{\text{bar}}$, the moving load may cause resonance between the beam and the elastic foundation because the beam behaves like a rigid bar at this speed, as shown in Fig. 3.2.

CHAPTER 4
MULTIDIMENSIONAL ANALYSIS

4.1 Introduction

Elastic wave propagation in a rail-foundation structure is essentially a 3D problem, but the Timoshenko beam model presented in Eqs. (2.11) and (2.12) simplifies it as a 1D waveguide problem under the assumption that deformed cross-sectional planes remain flat. If the cross-sectional dimensions of rails are small (i.e., thin beams), the dynamic effects of wave propagation on the cross-sectional plane may be negligible, but cross-sectional warpings can significantly affect structural stiffness and need to be accounted for [31, 33, 37]. Next we show the influences of cross-sectional warpings on the critical speed and other characteristic speeds by performing 2D sectional modeling and analysis. We factorize the rail's displacement field into one function describing the cross-sectional warping using 2D finite elements and one complex exponential function describing the wave propagating along the longitudinal axis (ignoring transverse wave propagation, i.e., waves traveling within the plane). This method is valid for computation of elastic waves of any wavelength.

4.2 Two-Dimensional Finite-Element Analysis of Cross-Sectional Warpings

Here we derive the wave propagation equations for an infinite, straight beam using the following extended Hamilton principle

$$\int_{t_1}^{t_2} \left(\delta T - \delta \Pi + \delta W_{nc} \right) dt = 0 \tag{4.1}$$

where T represents the kinetic energy, Π the elastic energy, and W_{nc} the non-conservative work from any external loading. For an arbitrary point on a cross section, its displacements are assumed to have the following form:

$$\begin{aligned} u_1(x,y,z,t) &= u(y,z)e^{j(\beta x-\omega t-\pi/2)} = -u(y,z)\,je^{j(\beta x-\omega t)} \\ u_2(x,y,z,t) &= v(y,z)e^{j(\beta x-\omega t)} \\ u_3(x,y,z,t) &= w(y,z)e^{j(\beta x-\omega t)} \end{aligned} \tag{4.2}$$

For this paper we are only concerned with waves propagating along the x direction (i.e. longitudinally), therefore $u(x,y,z,t)$ becomes $u(y,z)$ multiplied by the propagating wave in

the x direction $e^{j(\beta x-\omega t)}$. Then the linear strain-displacement relations can be obtained from Eq. (4.2) as:

$$\begin{cases} \varepsilon_{11}=u_{1x}=\beta u e^{j(\beta x-\omega t)} \\ \varepsilon_{22}=u_{2y}=v_y e^{j(\beta x-\omega t)} \\ \varepsilon_{33}=u_{3z}=w_z e^{j(\beta x-\omega t)} \end{cases},\quad \begin{cases} \varepsilon_{23}=u_{2z}+u_{3y}=(v_z+w_y)e^{j(\beta x-\omega t)} \\ \varepsilon_{13}=u_{1z}+u_{3x}=(\beta w-u_z)\,je^{j(\beta x-\omega t)} \\ \varepsilon_{12}=u_{1y}+u_{2x}=(\beta v-u_y)\,je^{j(\beta x-\omega t)} \end{cases} \tag{4.3}$$

The displacement u_1 being multiplied by -j in Eq. (4.2) is to assure the quadrature between u_1 and u_2 and u_1 and u_3, as shown by ε_{13} and ε_{12} in Eq. (4.3). For an orthotropic material, strains ε_{ij} are related to stresses σ_{ij} by the material stiffness matrix $[Q]$ as

$$\begin{Bmatrix} \sigma_{11} \\ \sigma_{22} \\ \sigma_{33} \\ \sigma_{23} \\ \sigma_{13} \\ \sigma_{12} \end{Bmatrix}=[Q]\begin{Bmatrix} \varepsilon_{11} \\ \varepsilon_{22} \\ \varepsilon_{33} \\ \varepsilon_{23} \\ \varepsilon_{13} \\ \varepsilon_{12} \end{Bmatrix},[Q]=\begin{bmatrix} Q_{11} & Q_{12} & Q_{13} & 0 & 0 & 0 \\ Q_{12} & Q_{22} & Q_{23} & 0 & 0 & 0 \\ Q_{13} & Q_{23} & Q_{33} & 0 & 0 & 0 \\ 0 & 0 & 0 & Q_{44} & 0 & 0 \\ 0 & 0 & 0 & 0 & Q_{55} & 0 \\ 0 & 0 & 0 & 0 & 0 & Q_{66} \end{bmatrix} \tag{4.4}$$

Hence, the variation of elastic energy of a beam segment having a length λ is given by

$$\begin{aligned} \delta\Pi &= \int_V \left(\sigma_{11}\delta\bar{\varepsilon}_{11}+\sigma_{22}\delta\bar{\varepsilon}_{22}+\sigma_{33}\delta\bar{\varepsilon}_{33}+\sigma_{23}\delta\bar{\varepsilon}_{23}+\sigma_{13}\delta\bar{\varepsilon}_{13}+\sigma_{12}\delta\bar{\varepsilon}_{12}\right)\mathrm{d}V \\ &= \int_V \begin{bmatrix} \beta^2(Q_{11}u\delta u+Q_{55}w\delta w+Q_{66}v\delta v) \\ +\beta\begin{pmatrix} Q_{12}(v_y\delta u+u\delta v_y)+Q_{13}(w_z\delta u+u\delta w_z) \\ -Q_{55}(u_z\delta w+w\delta u_z)-Q_{66}(u_y\delta v+v\delta u_y) \end{pmatrix} \\ +Q_{22}v_y\delta v_y+Q_{23}(w_z\delta v_y+v_y\delta w_z)+Q_{33}w_z\delta w_z \\ +Q_{44}(v_z\delta v_z+w_y\delta w_y+v_z\delta w_y+w_y\delta v_z)+Q_{55}u_z\delta u_z+Q_{66}u_y\delta u_y) \end{bmatrix}\mathrm{d}V \end{aligned} \tag{4.5}$$

where $\bar{\varepsilon}_{ij}$ denotes the complex conjugate of ε_{ij}. Moreover, the variation of kinetic energy is equivalent to the virtual work done by inertial forces $-\rho\ddot{u}_i$ as

$$\delta T=-\int_V \rho(\ddot{u}_1\delta\bar{u}_1+\ddot{u}_2\delta\bar{u}_2+\ddot{u}_3\delta\bar{u}_3)\mathrm{d}V=\omega^2\int_V \rho(u\delta u+v\delta v+w\delta w)\mathrm{d}V \tag{4.6}$$

Because there is no external loading (i.e., free vibration) and the problem domain contains exactly one wavelength λ, we have $\delta W_{nc}=0$. The 2D domain is then discretized using 2D shape functions for four-node quadrilateral elements as [38]

$$u=\{N\}^T\{u\}, v=\{N\}^T\{v\}, w=\{N\}^T\{w\}, \{N\}\equiv\{N_1, N_2, N_3, N_4\}^T$$
$$\{u\}\equiv\{u_1, u_2, u_3, u_4\}^T, \{v\}\equiv\{v_1, v_2, v_3, v_4\}^T, \{w\}\equiv\{w_1, w_2, w_3, w_4\}^T \tag{4.7}$$

Substituting Eq. (4.7) into Eqs. (4.5) and (4.6) and then into Eq. (4.1) and using the regular finite element assembly technique gives [37, 38]:

$$\left(\beta^2[K_2]+\beta[K_1]+[K_0]-\omega^2[M]\right)\{q\}=\{0\}$$
$$\{q\}\equiv\{u_1, v_1, w_1, \cdots, u_n, v_n, w_n\}^T, \{\hat{q}\}\equiv\{-u_1\mathrm{j}, v_1, w_1, \cdots, -u_n\mathrm{j}, v_n, w_n\}^T \tag{4.8}$$

where n is the total number of nodes and $\{q\}$ is the global displacement vector. To ease the solution process for the polynomial eigenvalue problem shown in Eq. (4.8) we rewrite it as

$$\left(\beta[\tilde{K}_2]+[\tilde{K}_1]\right)\{q\}=\frac{1}{\beta}\{q\},\ [\tilde{K}_i]\equiv\left[\omega^2[M]-[K_0]\right]^{-1}[K_i] \tag{4.9}$$

Then, Eq. (4.9) can be rewritten into the following standard eigenvalue problem:

$$\begin{bmatrix}[\tilde{K}_1] & [\tilde{K}_2]\\ [I] & [0]\end{bmatrix}\{\tilde{q}\}=\frac{1}{\beta}\{\tilde{q}\},\ \ \{\tilde{q}\}\equiv\begin{Bmatrix}\{q\}\\ \beta\{q\}\end{Bmatrix} \tag{4.10}$$

For a given vibration frequency ω, Eq. (4.10) gives $\beta=a_\mathrm{i}+\mathrm{j}b_\mathrm{i}$ (i=1,...,6n), but there are $3n$ repeated answers because of the definition of $\{\tilde{q}\}$ shown in Eq. (4.10). For the case that

$$\beta=\pm a, \{q\}\equiv\{\pm u_1, v_1, w_1, \cdots, \pm u_n, v_n, w_n\}^T,\ a>0 \tag{4.11}$$

it follows from Eq. (4.2) that it represents two propagative waves along the $+x$ and $-x$ directions, respectively. For the wave along the $+x$ direction, we have

$$u_{1\mathrm{i}}=u_\mathrm{i}e^{\mathrm{j}(ax-\omega t-\pi/2)}+u_\mathrm{i}e^{-\mathrm{j}(ax-\omega t-\pi/2)}=2u_\mathrm{i}\cos(ax-\omega t-\pi/2)=2u_\mathrm{i}\sin(ax-\omega t)$$
$$u_{2\mathrm{i}}=v_\mathrm{i}e^{\mathrm{j}(ax-\omega t)}+v_\mathrm{i}e^{-\mathrm{j}(ax-\omega t)}=2v_\mathrm{i}\cos(ax-\omega t) \tag{4.12}$$
$$u_{3\mathrm{i}}=w_\mathrm{i}e^{\mathrm{j}(ax-\omega t)}+w_\mathrm{i}e^{-\mathrm{j}(ax-\omega t)}=2w_\mathrm{i}\cos(ax-\omega t)$$

where $u_{2\mathrm{i}}$ denotes the u_2 of the ith node on the cross section. Eq. (4.12) shows that u_1 has a phase delay with respect to u_2 and u_3 by 90°. In other words, they are complex modes, and several continuous plots are needed in order to show their deformation sequence. However, at $ax-\omega t=\pi/4$, the deformed cross-sectional geometry $(u_{1\mathrm{i}}, u_{2\mathrm{i}}, u_{3\mathrm{i}})$ is proportional to $(u_\mathrm{i}, v_\mathrm{i}, w_\mathrm{i})$, and we will use this $(u_\mathrm{i}, v_\mathrm{i}, w_\mathrm{i})$ to demonstrate the deformed cross-sectional geometries later in Sec. 5.3. For the case that

$$\beta = \mathrm{j}b, \beta = -\mathrm{j}b,\ b > 0 \tag{4.13}$$

it represents two exponentially decaying evanescent waves along the $+x$ and $-x$ directions, respectively. For another case that

$$\beta = a + \mathrm{j}b\ \&\ \beta = -a - \mathrm{j}b,\ a,b > 0 \tag{4.14}$$

it represents two evanescent traveling waves along the $+x$ and $-x$ directions, respectively. For again another case that

$$\beta = \pm a - \mathrm{j}b, \{\hat{q}\} \equiv \{-\mathrm{j}(\pm u_1 - \tilde{u}_1\mathrm{j}), v_1 \mp \tilde{v}_1\mathrm{j}, w_1 \mp \tilde{w}_1\mathrm{j}, \cdots, -\mathrm{j}(\pm u_n - \tilde{u}_n\mathrm{j}), v_n \mp \tilde{v}_n\mathrm{j}, w_n \mp \tilde{w}_n\mathrm{j}\}^T, b > 0 \tag{4.15}$$

it represents an evanescent standing wave along the $-x$ direction. For the last case that

$$\beta = \pm a + \mathrm{j}b, \{\hat{q}\} \equiv \{-\mathrm{j}(\pm u_1 + \tilde{u}_1\mathrm{j}), v_1 \pm \tilde{v}_1\mathrm{j}, w_1 \pm \tilde{w}_1\mathrm{j}, \cdots, -\mathrm{j}(\pm u_n + \tilde{u}_n\mathrm{j}), v_n \pm \tilde{v}_n\mathrm{j}, w_n \pm \tilde{w}_n\mathrm{j}\}^T, b > 0 \tag{4.16}$$

it represents an evanescent standing wave along the x direction because, for example,

$$\begin{aligned} u_{2\mathrm{i}} &= (v_\mathrm{i} + \mathrm{j}\tilde{v}_\mathrm{i})e^{-bx+\mathrm{j}(ax-\omega t)} + (v_\mathrm{i} - \mathrm{j}\tilde{v}_\mathrm{i})e^{-bx-\mathrm{j}(ax-\omega t)} + (v_\mathrm{i} - \mathrm{j}\tilde{v}_\mathrm{i})e^{-bx+\mathrm{j}(-ax-\omega t)} + (v_\mathrm{i} + \mathrm{j}\tilde{v}_\mathrm{i})e^{-bx-\mathrm{j}(-ax-\omega t)} \\ &= 4\sqrt{v_i^2 + \tilde{v}_i^2}\, e^{-bx} \cos(ax + \theta)\cos\omega t, \quad \theta \equiv \tan^{-1}\frac{\tilde{v}_i}{v_i} \end{aligned} \tag{4.17}$$

All other modes are impossible exponentially growing modes. Of course, the most important modes are those propagative modes shown in Eq. (4.12).

CHAPTER 5

NUMERICAL RESULTS

5.1 Wave Numbers

For numerical studies we consider the medium caliber launcher (MCL) of the Institute for Advanced Technology for the reason that it is one of the most studied rail launchers in the world [39]. Its material and geometric properties are shown in Table 5.1.

Table 5.1: Properties of the MCL of the Institute for Advance Technology.

E = 120 GPa	G = 47 GPa	ρ = 8320 kg/m^3	k/b = 8.44 * 10^{11} N/m^3
b = 3.0 cm	h = 1.0 cm	I = 2.5 * 10^{-9} m^4	k = 5/6
V_c = 1355.3 m/s	V_{shear} = 2169.6 m/s	V_{bar} = 3797.8 m/s	

The four wave numbers from Eq. (3.15) are shown changing with the moving load speed v_0 ranging from zero to 12 km/s or approximately nine times the critical velocity in Figs. 5.1-5.3, where $a_1 \pm jb_1$ represents waveforms behind the load, and $a_2 \pm jb_2$ represents waveforms in front of the load. Values of a_2 and a_1 represent the exponential decay of a forward and backward wave respectively, hence a = 0 means there is no exponential decay of the wave and the possibillity of wave propagation. Values b_2 and b_1 represent the frequency of the waves in front of and behind the load, respectively and can give the wavelength through $\lambda = 2\pi/b$.

Figure 5.1 shows α over moving load speeds from zero to the shear speed. The dotted lines represent the imaginary numbers b_1 and b_2. For speeds less than V_c the real parts are symetrical about zero, and the imaginary parts are the same $b_1 = b_2$, i.e. the waveform is symmetric around the load. Since $a_1 > 0$ and $a_2 < 0$ there are no propagating waves in front of or behind the load. After the critical velocity (V_c=1355.3 m/s) the real parts become zero and the imaginary parts split. Therefore speeds above V_c have propagating waves because $a_1 = a_2 = 0$. If damping coefficient $c \neq 0$ then propagating waves will exponentially decay and only exist around the load. As v_0 increases towards the V_{shear}, b_2 approaches infinity and b_1 goes to a small finite number, hence the backward wavelengths become longer and the forward wavelengths become shorter because the

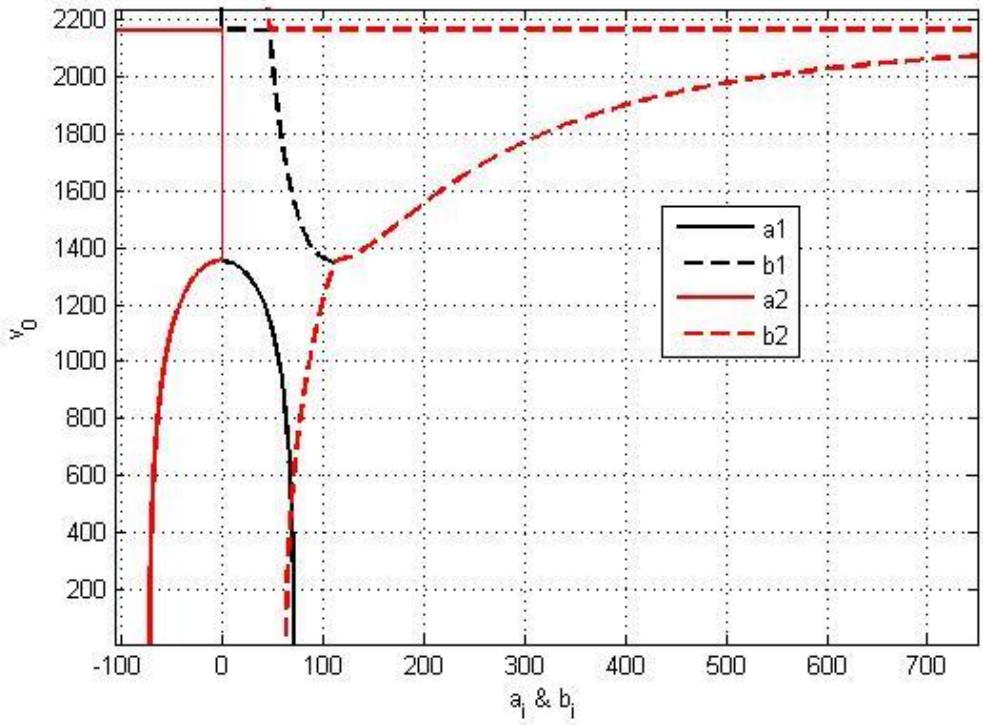

Figure 5.1: Wave numbers $a_i \pm jb_i (\equiv \alpha_i)$ for $v_0 < V_{\text{shear}}$.

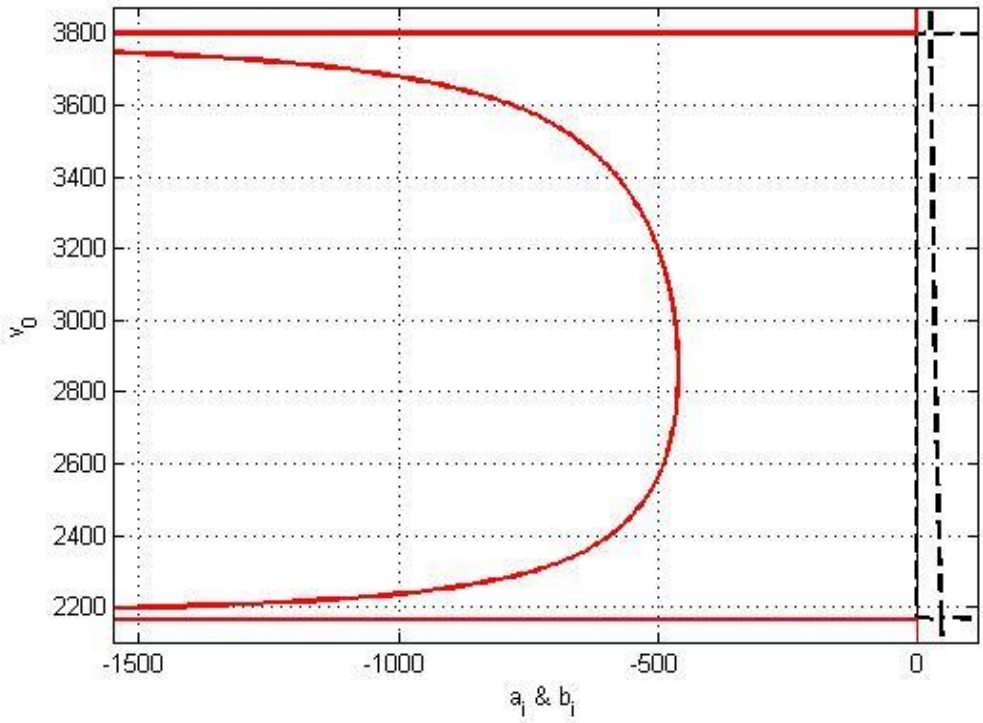

Figure 5.2: Wave numbers $a_i \pm jb_i (\equiv \alpha_i)$ for $V_{\text{shear}} < v_0 < V_{bar}$.

wave number is proportional to the frequency and inversely proportional to the wavelength ($\lambda=2\pi/b$).

If $V_{shear} < v_0 < V_{bar}$, Fig. 5.2 shows that $a_1 = b_2 = 0$ so there are propagating waves behind the load ($a_1=0$, $b_1\neq0$), and none in front of the load, i.e. no frequency since $b_2 = 0$. As the moving speed increases b_1 is a small positive number slowly decreasing, meaning the backward propagating wavelengths continue to steadily increase. On the other hand a_2 goes from negative infinity at V_{shear} to negative infinity at V_{bar}. With a_2 being a continuously a negative number and $b_2=0$, there is only a single non-oscillating exponentially-decaying wave in front of the load after V_{shear}. An unusual phenomenon exists in this forward exponential wave. Just above V_{shear} the exponential a_2 has a large value of -∞ (i.e. the wave decays quickly), but it approaches a smaller finite number between V_{shear} and V_{bar} then returns to -∞, meaning the exponential wave grows in size from V_{shear}=2169.6 m/s to $v_0\approx$2800 m/s and then decreases back before V_{bar}. There is no evidence as to why this occurs.

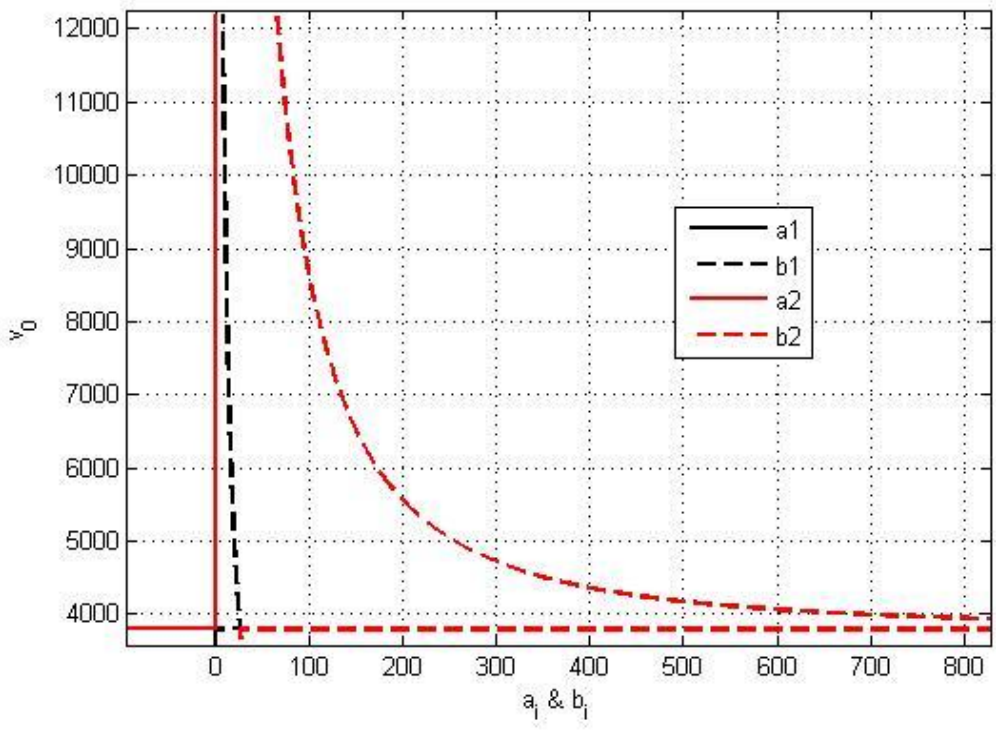

Figure 5.3: Wave numbers $a_i \pm jb_i (\equiv \alpha_i)$ for $v_0 > V_{bar}$.

Figure 5.3 has all values of α for moving load speeds greater than V_{bar} up to 12 km/s. After V_{bar} there are no real parts to the wave numbers (i.e., $a_1 = a_2 = 0$), b_1 is a small positive number that slowly decreases to zero, and b_2 starts from infinity and decreases towards zero as the moving load speed increases. Since b_1 and b_2 are non-zero, it seems that there are waves in front of and behind the load with different wavelengths, and the waves do not decay because $a_1 = a_2 = 0$. In reality b_1 and b_2 represent two unattenuated backward propagating waves with different frequencies because Eqs. (3.30) and (3.31) show that all the wave numbers now correspond to $s<0$. Therefore the beam has reached the phase velocity known as V_{bar}, and no waves exist in front of the moving load. b_2 now represents a backward propagating wave known as the longitudinal shear wave seen in Fig. 3.2. The shear wave has a smaller wavelength than the other backward propagating wave b_1 and shows high frequency extension/compression (optical mode) within the rail as discussed in Sec. 3.1. Again, larger moving load speeds continue to increase the wavelength of both of these waves.

5.2 Wave Forms

The waveforms corresponding to different values of v_0 are shown in Figs. 5.4 to 5.25. Fig. 5.4 shows the waveform of the rail for the armature speed at 0.5 times the critical velocity. The x-axis is the distance along the rail where s=0 represents the position of the moving load. As we can see from the model the largest deformation is at s=0 – the location of the moving load, and the waves are quickly damped moving away from the load. Knowing the basic waveform below critical speed, the physical changes in the waveform can be seen in Figs. 5.5, 5.6, and 5.7 showing $v_0 = 0.7V_c$, $0.9V_c$, and $0.98V_c$ respectively. These figures show an increasing max amplitude at the load, a decreasing exponential decay, and a shortening of the wavelength as the v_0 approaches V_c. Note that the amplitude and wavelength in front of and behind the load are the same for all variables because the real part of the wave numbers have symmetry about zero $a_1=-a_2$, and the imaginary parts are equal $b_1=b_2$.

After the critical speed the waves begin to propagate forwards and backwards along the rail (i.e. $a_1=a_2=0$). The new waveform appears as shown in Fig. 5.8 for

v_0=1.05V_c. This waveform is consistent for armature speeds between the critical and shear speeds. As the velocity increases between the critical and shear speeds, b_1 decreases and b_2 increases, and hence the wavelengths in front of the armature decrease while the wavelengths behind the armature increase. Moreover, the amplitude of all waves decreases. Figures 5.8-5.13 show how the waveforms change between the critical and shear speeds. After the critical speed we notice that all wave amplitudes are decreasing with increasing speeds whereas the wavelengths move in opposite directions with the forward wavelengths decreasing and the backward wavelengths increasing. Concurrently, we notice that ψ has the same amplitude in front of and behind the armature for all speeds between critical and shear velocity.

Another waveform transformation, and possibly the most drastic waveform change, happens after the shear speed is reached. After the shear speed, waves no longer propagate in front of the moving load (given b_2=0). A single exponentially decaying, non-oscillating wave exists in front of the armature (a_2<0), while the backward waves continue to grow with increases in speed. The waveform right beyond the shear speed is depicted in Fig. 5.14. Figs. 5.14-5.19 show the change in amplitude and wavelength when $V_{\text{shear}} < v_0 < V_{\text{bar}}$.

Once the bar speed is reached, there is no longer any waves in front of the moving load as no elastic waves are capable of propagating in front of the load. Two more notable transformations occur above bar speed; the backward wave takes on an extra harmonic wave due to the development of a short-wavelength shear rotation known as the longitudinal shear wave, and ψ and γ, which have been in phase from the starting velocity v_0=0 now become out of phase by 180° - in other words, the bending-shear coupling went from a forward propagating low energy mode (acoustic mode) to a backwards high energy mode (optical mode). This deformation pattern can be seen in Fig. 3.2 and is supported by the deformations shown in Figs. 5.20-5.25. These figures show the waveforms for speeds up to $3V_{bar}$ (≈12 km/s).

We can see that although v_0 is greater than V_{bar} waves still exist behind the load. This means a constant load moving at a speed higher than V_{bar} can drag a deformed wave profile to move faster than V_{bar}. As a real armature has multiple points of contact with the

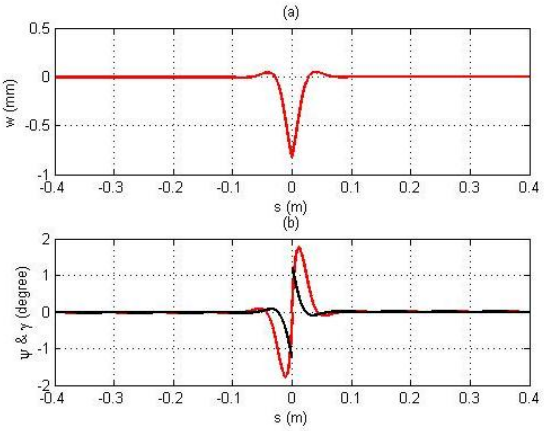

Figure 5.4: Waveform at $0.5V_c$.

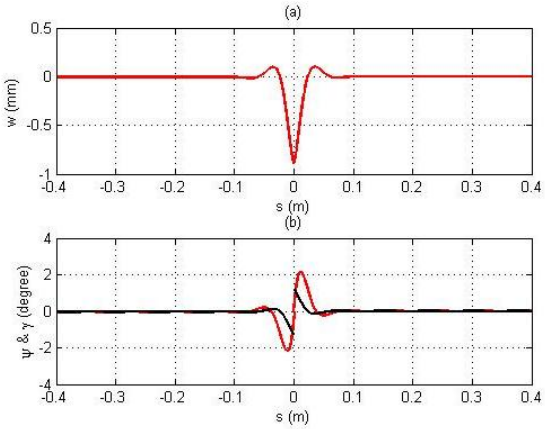

Figure 5.5: Waveform at $0.7V_c$.

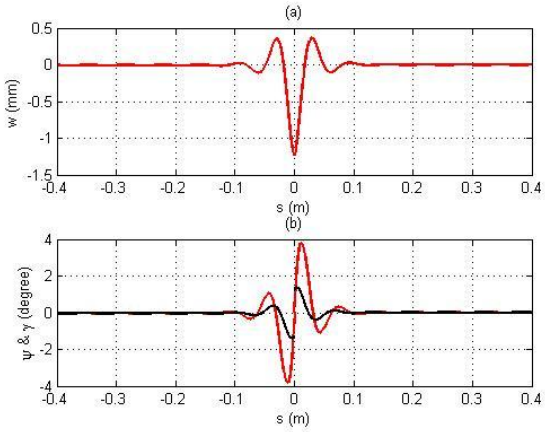

Figure 5.6: Waveform at $0.9V_c$.

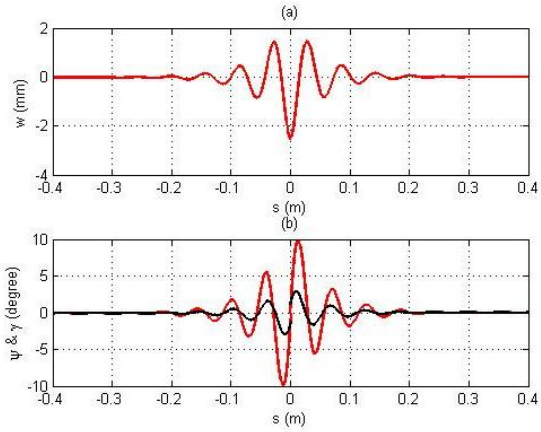

Figure 5.7: Waveform at $0.98V_c$.

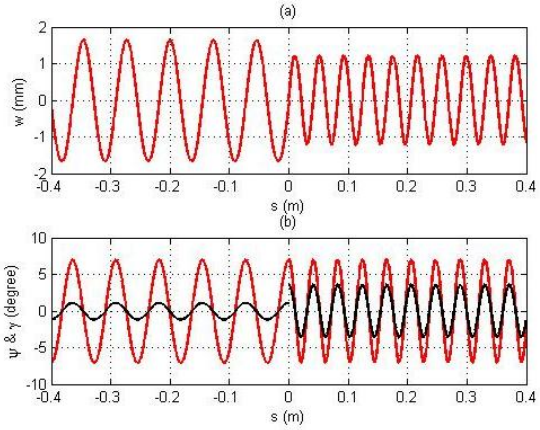

Figure 5.8: Waveform at $1.05V_c$.

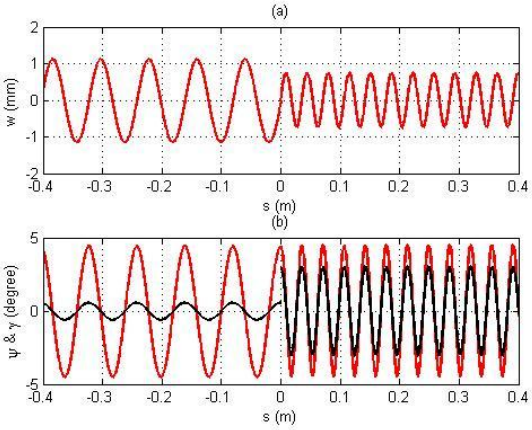

Figure 5.9: Waveform at $1.1V_c$.

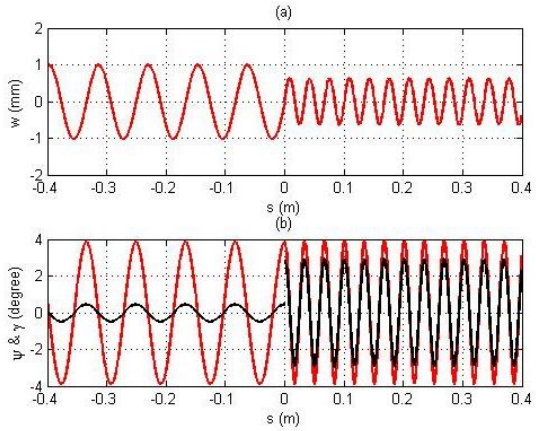

Figure 5.10: Waveform at $0.7V_{shear}$.

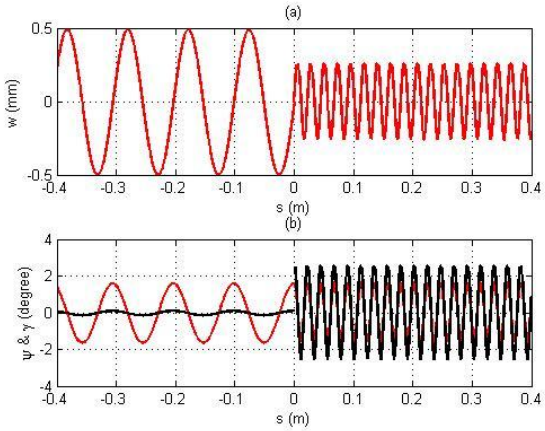

Figure 5.11: Waveform at $0.8V_{shear}$.

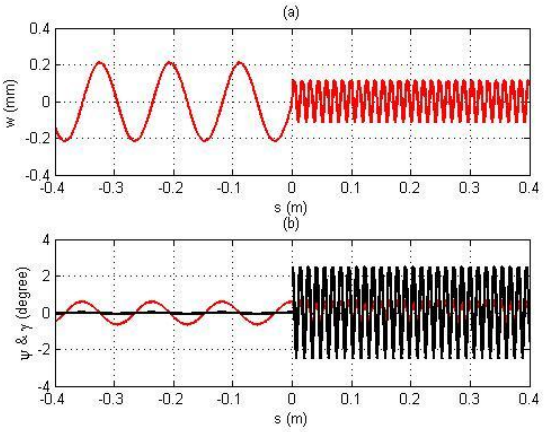

Figure 5.12: Waveform at $0.9V_{shear}$.

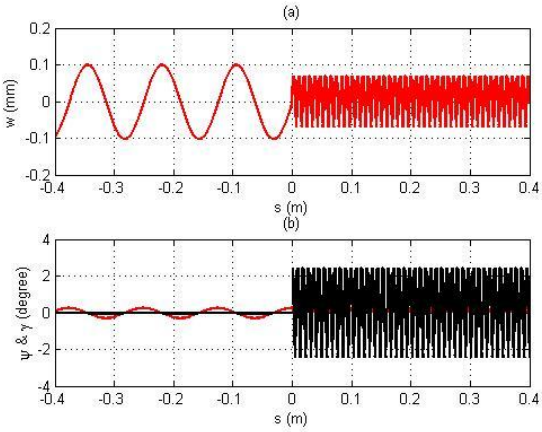

Figure 5.13: Waveform at $0.95V_{shear}$.

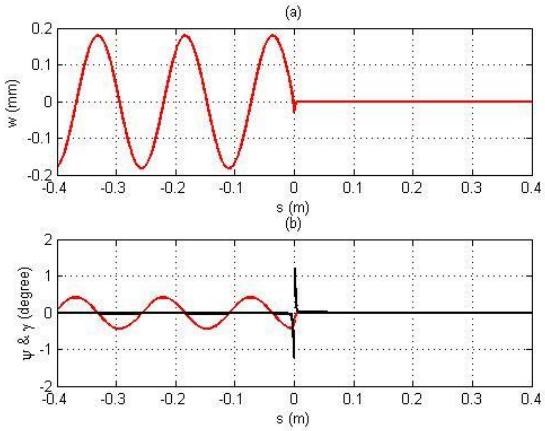

Figure 5.14: Waveform at $1.1V_{shear}$.

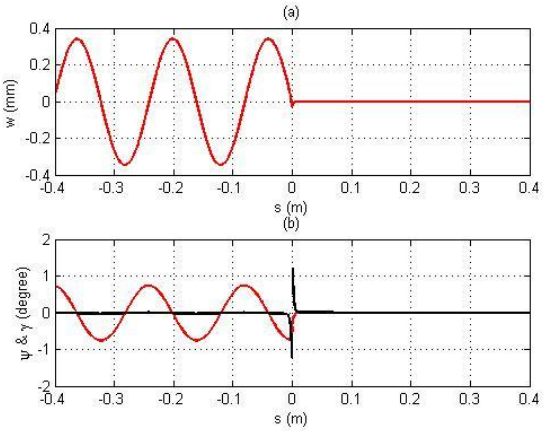

Figure 5.15: Waveform at $1.2V_{shear}$.

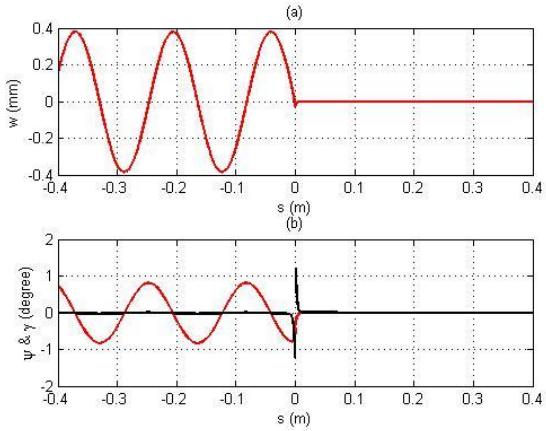

Figure 5.16: Waveform at $0.7V_{bar}$.

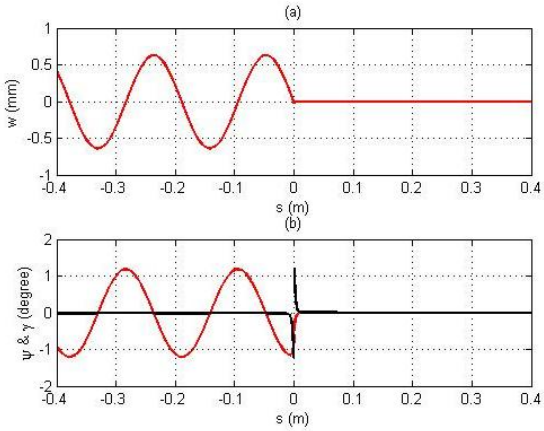

Figure 5.17: Waveform at $0.8V_{bar}$.

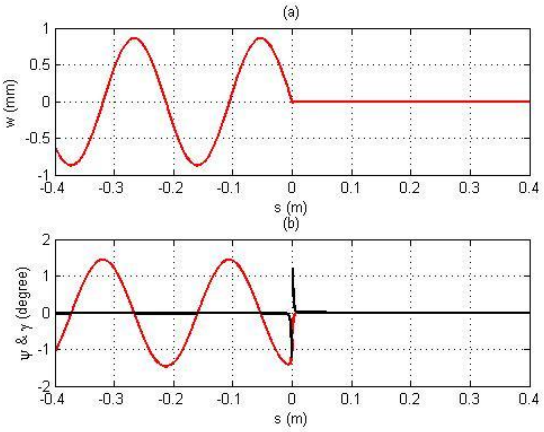

Figure 5.18: Waveform at $0.9V_{bar}$.

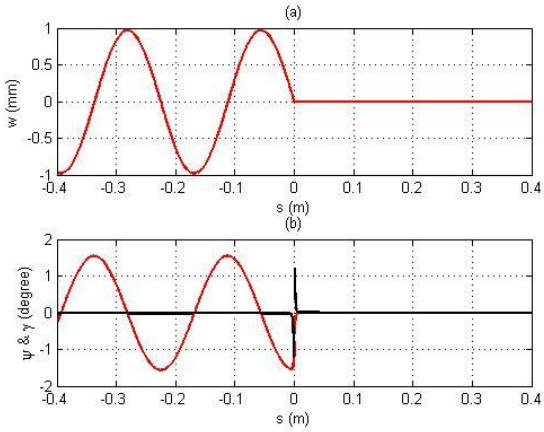

Figure 5.19: Waveform at $0.95V_{bar}$.

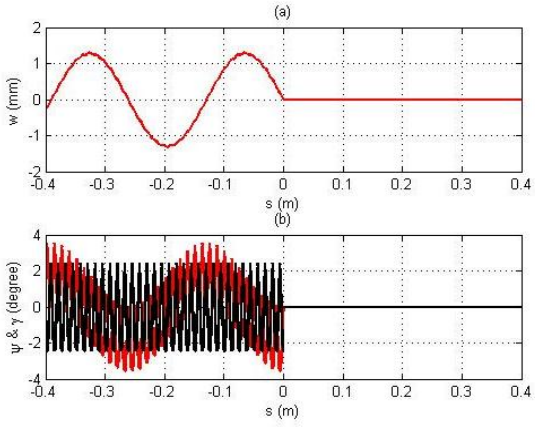

Figure 5.20: Waveform at $1.1V_{bar}$.

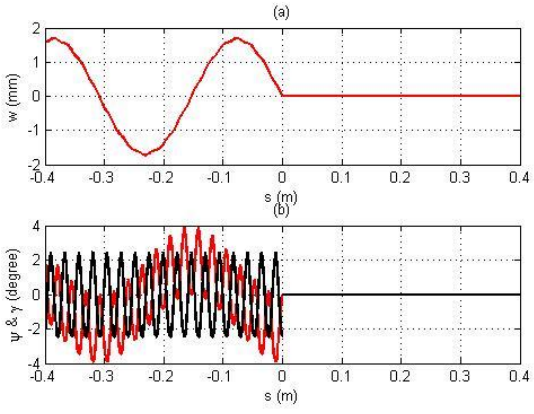

Figure 5.21: Waveform at $1.3V_{bar}$.

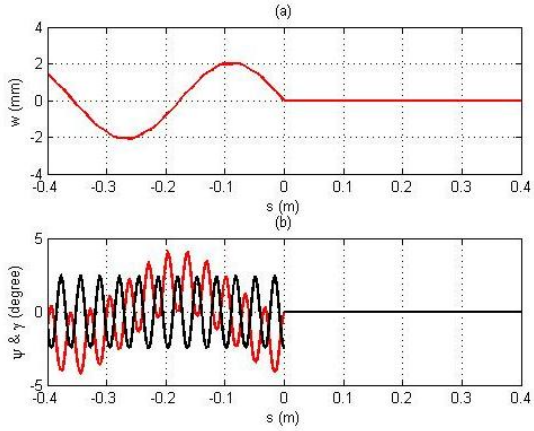

Figure 5.22: Waveform at $1.5V_{bar}$.

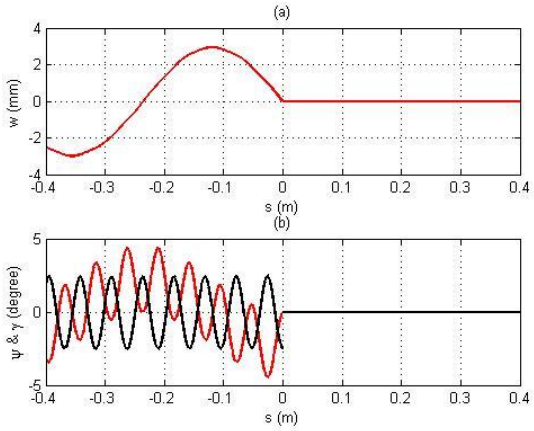

Figure 5.23: Waveform at $2.0V_{bar}$.

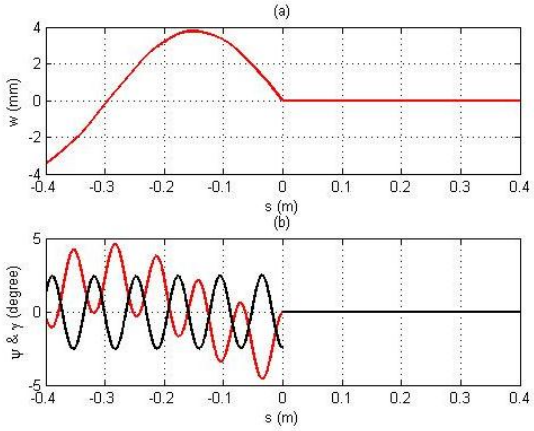

Figure 5.24: Waveform at $2.5V_{bar}$.

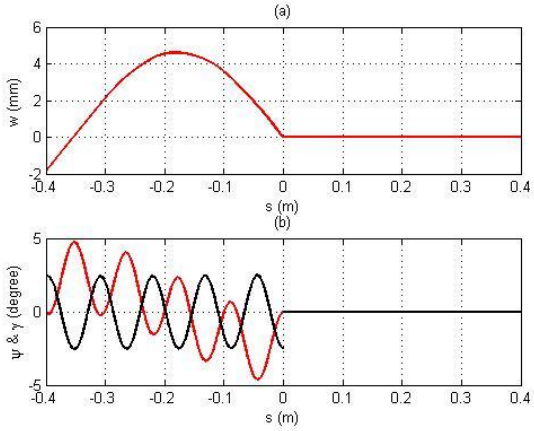

Figure 5.25: Waveform at $3.0V_{bar}$.

rails, the deformation of the backward wave becomes bumpy from the front contact points and will cause impacts at rear contact points causing rail damage.

Keeping in mind the differences in waveforms between each of the characteristic speeds, Figs. 5.26-5.29 show the max amplitude and wavelengths of the waves in the rails for all speeds up to 12 km/s, or about nine times the critical velocity. From these figures we can see potential problematic speeds for railgun launches; the discontinuity of the amplitudes of w, ψ, and γ at V_c from parametric excitation (discussed next) and the large deformations at higher speeds. As the armature speed increases the waves seem to grow in an almost linear fashion after V_{shear}.

To help explain what the critical frequency is we examine the cut-on frequency obtained from $\hat{R} = 0$ in Eq. (3.10) from the Timoshenko model. Figures 5.31 and 5.32

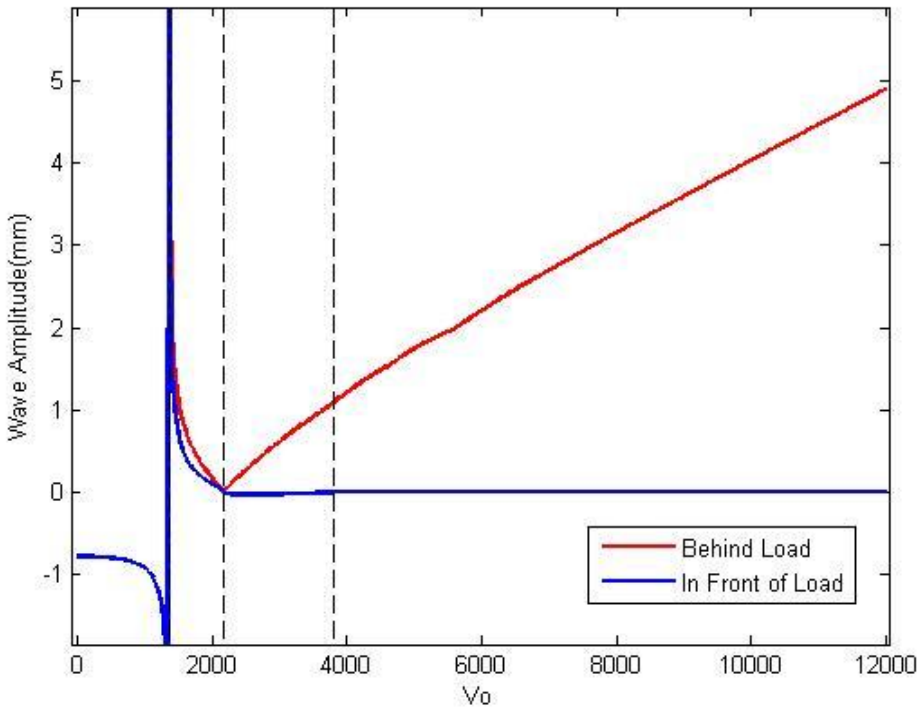

Figure 5.26: Peak displacement of *w* for all speeds up to 12 km/s.

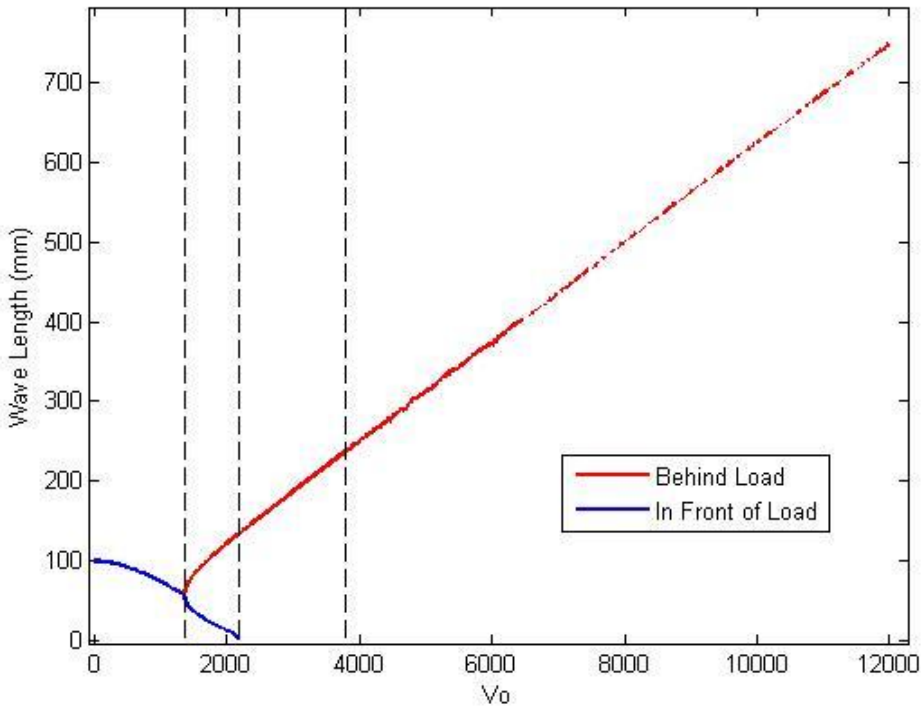

Figure 5.27: Wavelengths of *w* for all speeds up to 12 km/s.

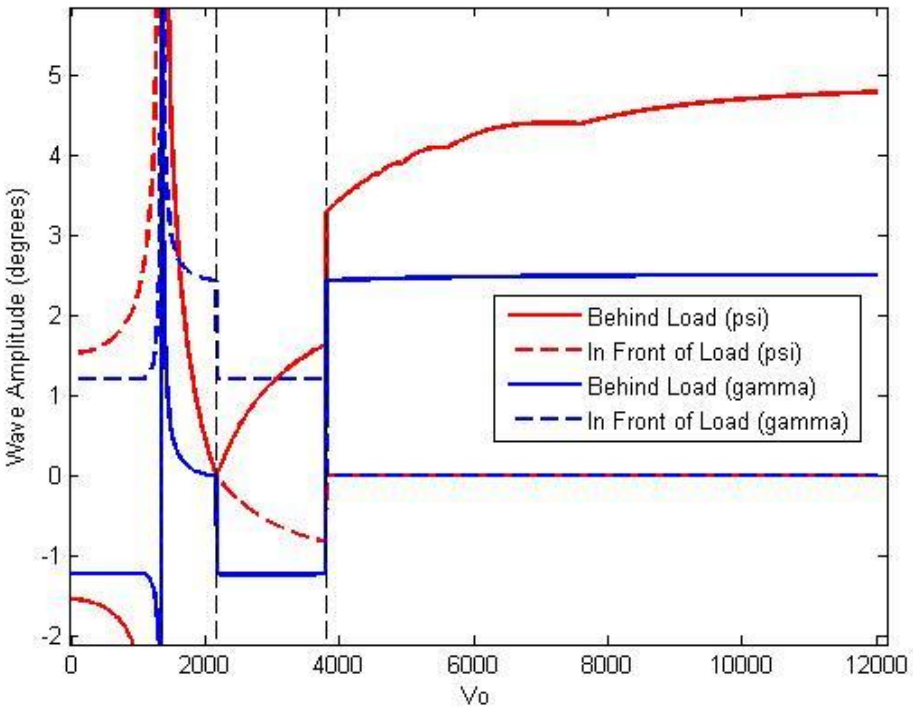

Figure 5.28: Peak displacements of ψ and γ for all speeds up to 12 km/s.

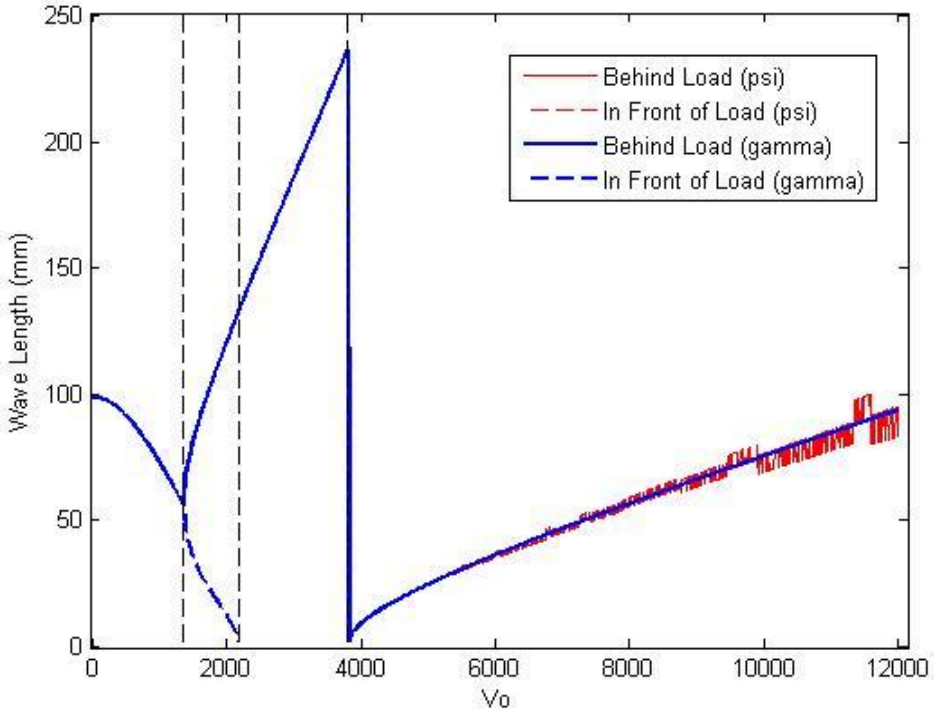

Figure 5.29: Wavelengths of ψ and γ for all speeds up to 12 km/s.

shows the dispersion cures ω-V and ω-β respectively. When the excitation frequency changes, the corresponding wave velocity and wave number change, where $\omega_{\text{cut}} = 16017.4$ Hz. At ω_{cut} we have $V_{\text{cut}} \to \infty$, $\beta_{\text{cut}} = 0$, and $\lambda_{\text{cut}} \to \infty$ (since λ=2π/β). This is an impossible propagative wave because $V_{\text{cut}} > V_{\text{bar}}$, and hence the cut-on frequency cannot be used to explain the critical speed. On the other hand if the wave frequency increases to $\omega_c = 24207$ Hz, the corresponding phase velocity obtained from Eq. (3.10) is V_c=1355.3 m/s and the wave number is $\beta_c = 112.22$ rad/m. As shown in Fig. 5.31, it is the minimum free-wave phase velocity, and it is called the critical speed because an armature starting from zero velocity will reach this speed first. After the armature reaches this speed, if it accelerates further and there is only one contacting point between the rail and armature, it needs to climb over and hence resonate with the deformed beam geometry causing parametric excitation. The waveforms shown in Figs. 5.8 through 5.13 are parametrically excited vibrations. However, a real armature as seen Fig. 5.30 always has two or more points contacting with the rails. If the characteristic contacting length is ℓ, the armature will intend to excite the rail at a frequency $\Omega = V / \ell$ due to disturbing forces caused by the random roughness of contacting surfaces. This is known as forced excitation and hence, even when the armature speed is less than V_c, rail vibration is expected, especially when Ω is close to one of the natural frequencies of the rail-foundation system. When the armature speed reaches V_c the forced excitation frequency ($= V_c / \ell$, e.g., Point #1 on Fig. 5.31) is higher than the parametric excitation frequency ($= V_c / \lambda_c = \omega_c$). When the wavelength decreases to $\lambda = \ell$, a worse vibration happens because the rail is subject to both parametric and forced excitations at the same frequency (i.e., Point #2 on Fig. 5.31). If the excitation frequency is also equal to a natural frequency of the armature-rail system, the situation is even worse. Therefore, the armature length plays an important role in the design of railgun dynamics. Figure 5.31 also shows that there are two different ω values corresponding to one velocity value. The lower one is for the backward propagating wave and the higher one is for the forward propagating wave (again see Figs. 5.8 through 5.13).

The broken straight line in Fig. 5.32 represents the dispersion curve of a non-dispersive material, and it tangents to the dispersion curve of the rail-foundation system at the critical frequency ω_c. When the wave speed increases from zero, the broken straight line rotates clockwise with respect to the origin at $(\omega, \beta) = (0, 0)$ until it touches the $\omega - \beta$ curve at ω_c.

Note that the amplitudes of the forward and backward radiating shear rotation waves shown in Figs. 5.20-5.25 and Fig. 5.28 above V_{bar} are all about 2.4° $(= -F/(\kappa GA))$, and the shear rotations introduce the small local bumps to the backward transverse waves. Hence, shear rotation plays an important role in the wave dynamics of railguns when $v_0 > V_c$, and it is important to have accurate modeling of shear rotation. However, when shear rotations are significant, Figures 3.1 and 3.2 show that the assumed, flat deformed cross- sections are too much restrained because Timoshenko's beam theory uses only two variables (i.e., w and ψ) to describe the deformation of a beam, which is essentially a 3D solid in nature, especially at high frequencies.

To improve the beam theory by accounting for 3D stress effects one can adopt a higher-order shear-deformable beam theory using more than two displacement variables to describe the out-of-plane and in-plane cross-sectional warpings, such as a layer-wise beam theory or a sublamination beam theory [31, 32, 40]. The generalized dynamic stiffness method shown in Eqs. (3.20)-(3.22), (3.29), and (3.31) can be easily extended to deal with such beam theories with more displacement variables. However, the number of resulted governing partial differential equations increases with the number of displacement variables. One way to reduce the number of displacement variables in a high-order beam theory that accounts for 3D stress effects is to use just a small number of important cross-sectional warping modes from 2D cross sectional analysis [41, 42].

From Section 3.2 we derived the critical speed formula as shown in Eq. (3.27), which is nonlinear in nature. As the pre-compression (N>0) decreases, the critical speed will increase with most square of the Pre-compression N. Figure 5.33 shows the effect of the pre-compression load on the critical speed. Due to our directional assumption from Section 3.2, N>0 means a compression load while N<0 is a tension load. From this we can clearly see that applying a tension load can increase the critical speed, and even

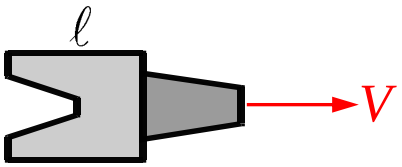

Figure 5.30: Railgun armature.

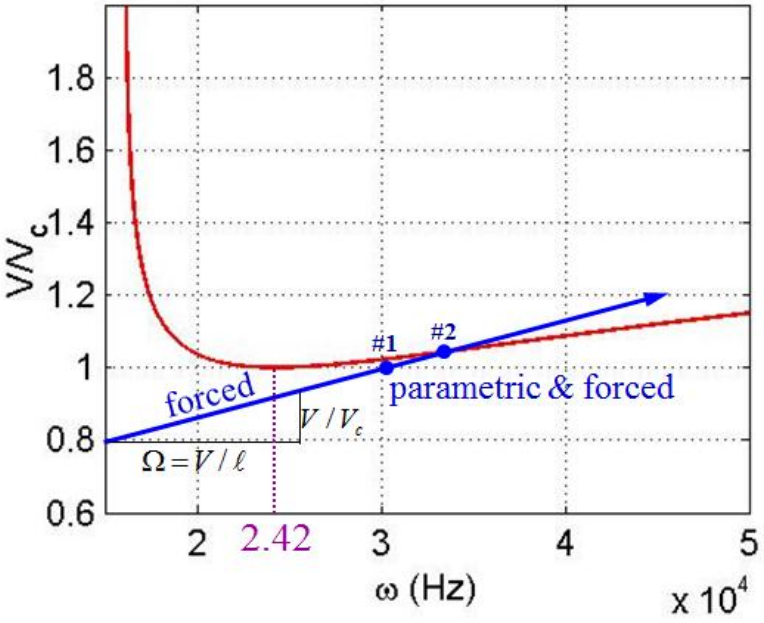

Figure 5.31: The $\omega - V$ dispersion curve.

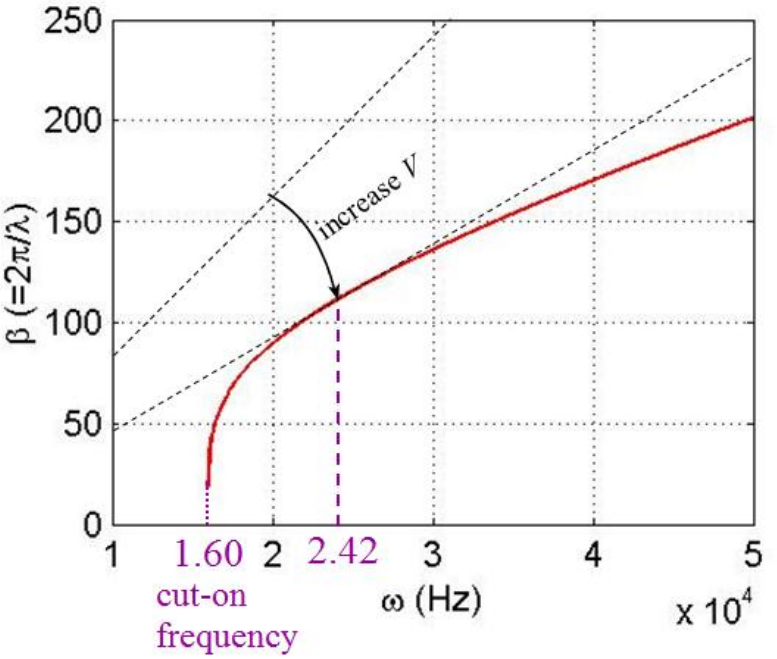

Figure 5.32: The $\omega - \beta$ dispersion curve.

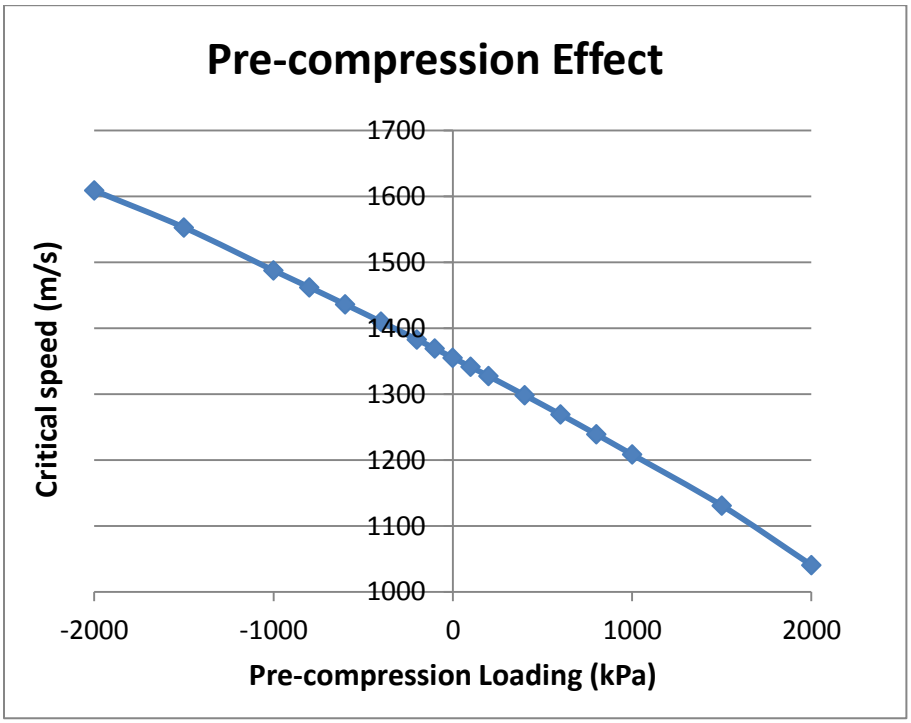

Figure 5.33: Change in the critical speed with respect to pre-compression loading.

though Eq. (3.27) is nonlinear, the resulting change in critical speed is almost linear over a range of ±600 kPa with a rate of -0.139 (m/s)/(kPa). Using this, we can increase the critical speed and decrease the period between the critical and shear speed, i.e. decrease the time and range of speeds at which forward deformation waves propagate.

5.3 Influences of Cross-Sectional Warpings

First we perform the cross-sectional analysis derived in Chapter 4 using the rail properties shown in Table 5.1 without the elastic foundation. Using 200 4-node quadrilateral elements with 231 nodes and 693 degrees of freedom (DOFs) the cross-sectional mesh is shown in Fig. 5.34. Figure 5.35 shows the dispersion curves of the six propagative waves that exist below 60 kHz. The frequency range 0 to 60 kHz was used because we chose to ignore in-plane propagating waves in the y and z directions in Eq. (4.2). Therefore wavelengths shorter than the cross-plane dimensions b and h will not be used. Under these assumptions the propagating waves in the x-direction, longitudinally, are the longitudinal wave (the bar-mode), the transverse waves due to bending with

respect to the y and *z* axes (*b2* and *b3* respectively), local bending around the x axis (b1), the torsional wave (t-mode), and the shearing on the *xy* plane (the s-mode). When the vibration frequency is $\omega = 40$ kHz, the deformation patterns of the six mode shapes are shown in Fig. 5.38. Under these conditions no explanation for any critical velocities can be seen.

When an elastic foundation is added in the z-direction to account for the G-10 insulator, the same mode shapes exist below 60 kHz. The G-10 insulator properties in Table 5.1 are used. Figure 5.36 shows the effect of the z-direction elastic foundation on the dispersion curves, and Fig 5.39 shows the six mode shapes of the rail with a foundation at 40 kHz. Comparing Figs. 5.35 and 5.36, some shifting of the mode velocities and wavelengths is observed. For example, at 40 kHz without the foundation, V_{bar} = 3,713.6 m/s, V_s = 32,383 m/s, and V_{b1} = 3,989.4 m/s, whereas with the foundation, V_{bar} = 3,715.7 m/s, V_s = 32,399 m/s, and V_{b1} = 5,467.1 m/s. The significant difference in a rail with an elastic foundation is the b_2 and t-modes cut-on frequency is no longer zero. While $\omega_{cut}=0$ for b_2 and t-modes on a free rail as seen in Fig 5.35, Fig. 5.36 shows $\omega_{cut} \approx 15$ kHz for a rail on an elastic foundation.

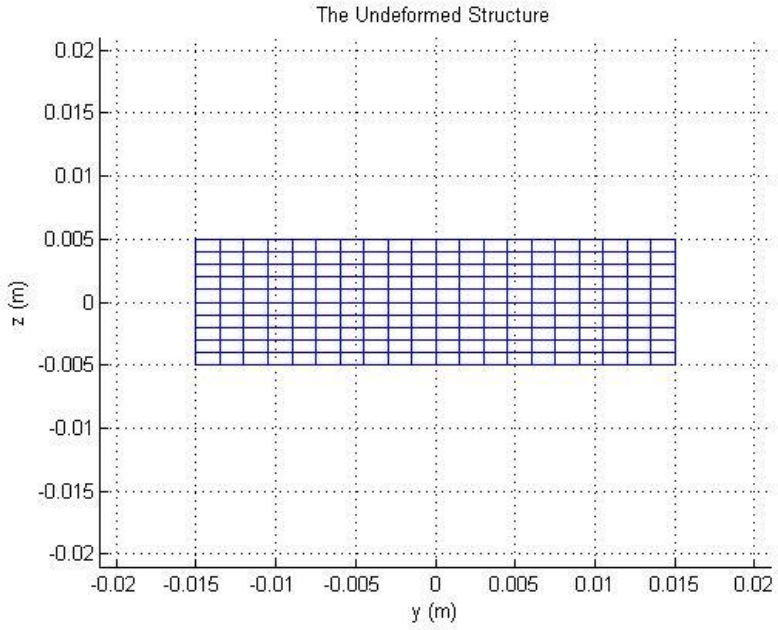

Figure 5.34: The 2D cross-sectional mesh used for FEA.

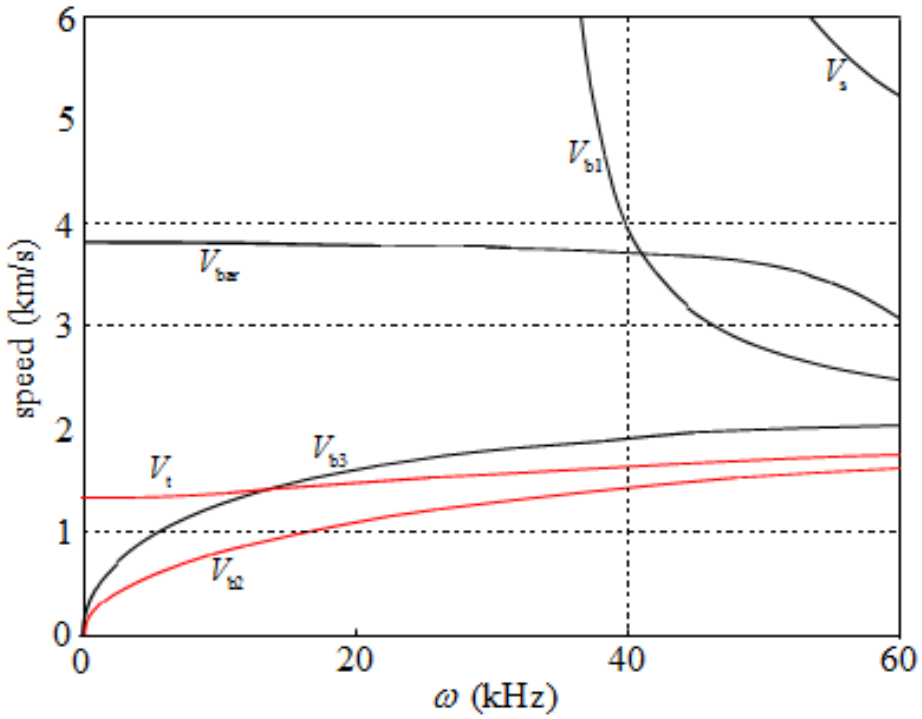

Figure 5.35: Dispersion curves of propagating modes without foundation.

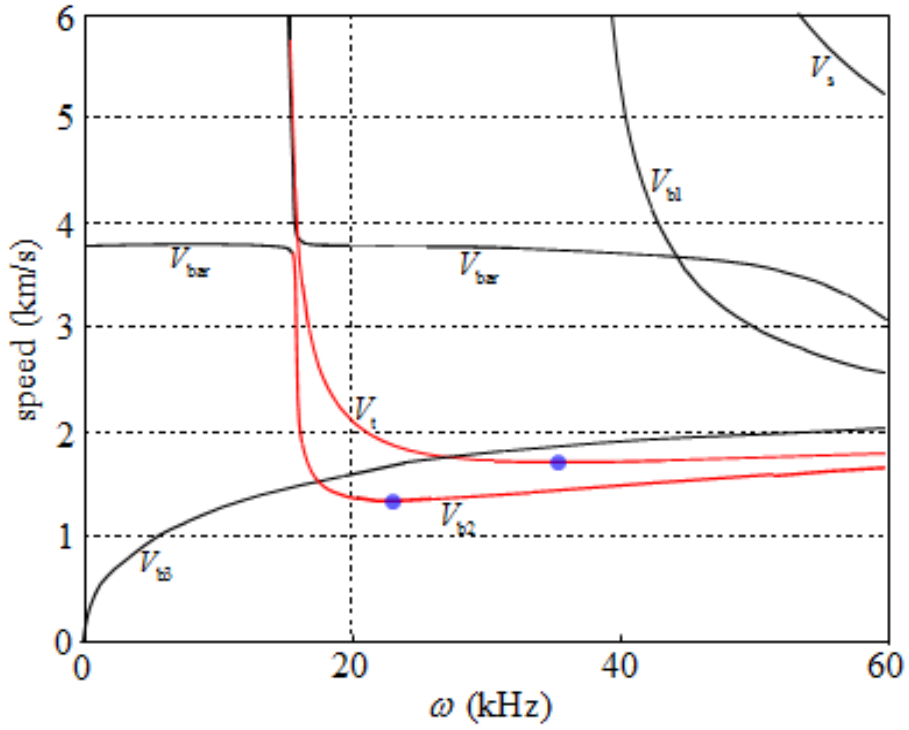

Figure 5.36: Dispersion curves of propagating modes with foundation.

Figure 5.37 a, b, c, and d show the deformed 3D cross-sectional geometries and their 2D projections of the four propagative waves in a rail without foundation when the vibration frequency is ω=10 kHz. Conversely, Fig. 5.37 e and f show the two propagative waves when ω=10 kHz when a foundation exists. There are two things to note from Fig. 5.36. The cut-on frequency of the b_2 and t modes is greater than 10 kHz when the rail is on an elastic foundation. Hence, there is no b_2 or t mode at 10 kHz for the rail with foundation, and the wave traveling speed and wavelength of the other modes are similar for the rail with and without the foundation. This also holds true in Figs. 5.38-5.41 that show the modes with and without foundations at 40 kHz and 60 kHz respectively.

Comparing Figs. 5.38 and 5.39 to Figs. 5.40 and 5.41 shows that, when the frequency increases, the wavelengths decrease and the in-plane warping displacements increase. At the same time, we see that out-of-plane warpings become restrained at higher frequencies. The most significant change of the cross-sectional geometry happens to the bar-mode. Results show that the cross-section remains flat at low frequencies, but the cross section is curved with respect to the *z*-axis at a high-frequency vibration, as shown in Figs. 5.37 a, e, 5.38 c, 5.39 c, 5.40 b, and 5.41 b. Figures 5.39 and 5.41 also show that the shear warping of the b_3 and b_2-modes becomes more severe when the vibration frequency increases. Moreover, the out-of-plane torsional warping displacements of the t-mode increase when the vibration frequency increases.

At low frequencies, the four propagative wave speeds can be estimated using the Euler-Bernoulli beam theory as

$$V_{bar}=\sqrt{\frac{E}{\rho}}=3797.8 \text{ m/s},\ V_t=\sqrt{\frac{GI_1}{J}}=1336.0 \text{ m/s},\ V_{b2}=\left(\frac{EI_2}{m}\right)^{1/4}\sqrt{\omega},\ V_{b3}=\left(\frac{EI_3}{m}\right)^{1/4}\sqrt{\omega}$$
$$I_1=\frac{bh^3}{3}\left(1-\frac{192h}{\pi^5 b}\sum_{n=1,3,\ldots}^{\infty}\frac{1}{n^5}\tanh\frac{n\pi b}{2h}\right), I_2=\frac{bh^3}{12}, I_3=\frac{b^3h}{12} \tag{5.1}$$

where the torsional area moment of inertia, I_1, is obtained from the theory of elasticity to account for the influence of torsional warping [33]. At low frequencies, the values of V_{bar} and V_{t} from sectional analysis agree well with the two fixed values from Eq. (5.1). However, Figs. 5.35 and 5.36 show that, when the cross-sectional warpings increase with

the frequency, V_{bar} decreases because cross-sectional deformations like the b_1 and s-mode provide extra local degrees of freedom to absorb the dynamic energy and hence slows down the forward propagating speed. On the other hand, V_t increases with the frequency because in general out-of-plane warping displacements are more restrained at high frequencies. Moreover, these two elastic waves become dispersive at high frequencies. These phenomena may not be important for common low-frequency vibration problems, but it needs to be considered for railgun dynamics because the armature speed of railguns can be up to 10 km/s [6].

For the transverse modes b_2 and b_3, when ω increases, Figs. 5.37-5.39, show that, under a flexural vibration, shear deformation of the cross section becomes more significant when the frequency and/or the thickness increases. At $\omega = 20$ kHz, the three values of V_{b2} obtained from the sectional analysis (Chapter 4 without a foundation), Timoshenko's beam theory (Eq. (2.13)), and the Euler-Bernoulli beam theory (Eq. (5.1)) are 1081.9, 1072.0, and 1173.7 m/s, respectively. At $\omega = 60$ kHz, the three values of V_{b2} are 1621.1, 1594.0, and 2033.0 m/s, respectively. We can see that the Bernoulli-Euler model diverges at high frequencies, which is expected as examined in Sec. 2.3. However, analysis from the Timoshenko and 2D cross-sectional model agree well with each other. Furthermore, at $\omega = 20$ kHz, the three values of V_{b3} are 1607.1, 1594.8, and 2033.0 m/s, and at $\omega = 60$ kHz, the three values of V_{b3} are 2038.5, 2005.2, and 3521.2 m/s, respectively. It is obvious that the Euler-Bernoulli beam theory is not accurate for high-frequency analysis due to its dramatic divergence, and the use of the shear correction factor κ in Timoshenko's beam theory is able to appropriately account for the shear warping effect at high frequencies. However, the frequency from the sectional analysis is slightly higher than that from Timoshenko's beam theory because the cross-sectional warping is restrained during high-frequency vibration.

Figures 5.36, 5.37, and 5.39 show that the b1-mode and the s-mode have non-zero cut-on frequencies because they are local deformation modes behaving like elastic waves in an elastic material sitting on an elastic foundation. For the b_3-mode shown in Figs. 5.38 d and 5.39 d, its bending rotation is in phase with its shear rotation (i.e., an acoustic mode, see ψ and γ in Figs. 5.10-5.13). On the other hand, the bending rotation and the

shear rotation of the s-mode shown in Fig. 5.38 a and 5.39 a are 180° out of phase (i.e., an optical mode, see ψ and γ in Figs. 5.22-5.25).

It shows in Fig. 5.36 that the elastic foundation makes the wave speed of the longitudinal wave discontinuous around 15800 Hz. The elastic foundation also changes the cut-on frequency of the b_1-mode from 34662 Hz in Fig. 5.35 to 36850 Hz in Fig. 5.36, and that of the s-mode from 39654 Hz to 39641 Hz. The elastic foundation makes the t-mode and the b_2-mode have cut-on frequencies at 15135 Hz and 15864 Hz, respectively. Figure 5.36 shows that the b_2-mode has a critical speed (the lowest speed at which a b_2-mode wave can propagate) of 1347.6 m/s at 23510 Hz, which agrees well with those shown in Fig. 5.31 from Timoshenko's beam theory. More importantly, the torsional mode introduces another critical speed of 1715.8 m/s at 36000 Hz. Just like the critical speed of the b_2-mode, this critical speed of the t-mode may play an important role in railgun dynamics.

Furthermore, the G-10 insulator provides electrical insulation from the containment in the y direction as well. Adding another elastic foundation to our rail cross-sectional model in the y-direction provides another implication. Figure 5.42 shows the new rail dispersion curves. From the figure the elastic foundation in the y-direction adds another critical frequency. There are actually three critical speeds; not only those of the b2 and torsional modes, but the b3 mode now has a cut-on frequency of $\omega_{cut\text{-}on}$ = 12745 Hz and a critical speed of 1852.4 m/s at 21028 Hz. While the b3 mode by itself is a transverse deformation that is not in the direction of the armature, interaction between the propagating waves of these three critical speeds can cause seemingly random vibrational patterns in all directions. This may be why the armature can lose contact with the rail and help to explain armature transitioning. As previously mentioned, armature transitioning occurs in low velocity shots (< 2 km/s) [8-12]. Under 2 km/s there are three critical speeds of a rail on an elastic foundation, i.e., there are three deformation patterns propagating away from the moving load at these speeds. Furthermore, forward propagating waves can induce bouncing as the accelerating armature travels over them, and possibly result in loss of armature and rail contact through pitch, roll, and yaw of the armature - i.e. armature transitioning.

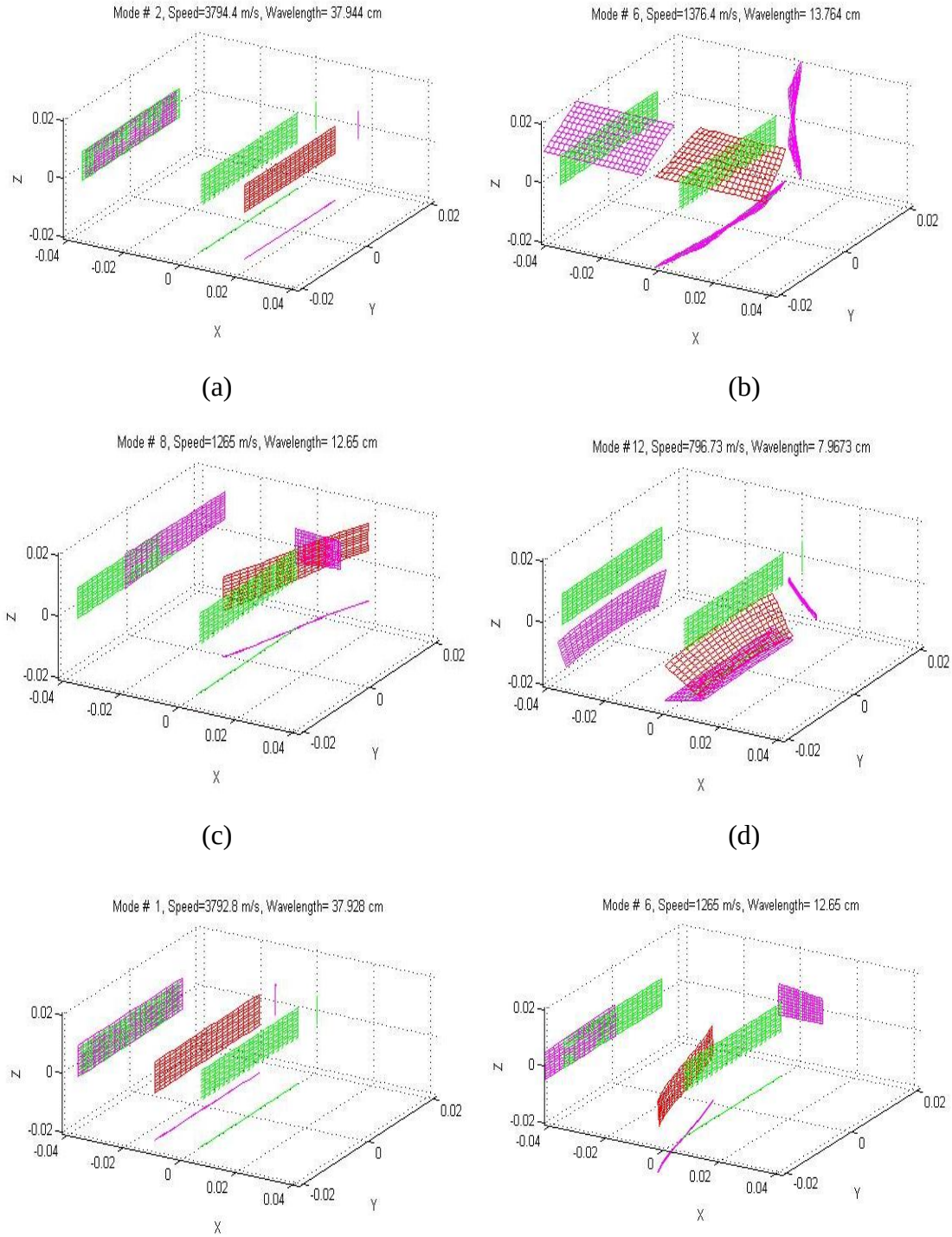

Figure 5.37: The deformation mode shapes at 10 kHz: (a,b,c,d) bar, torsion, b3, and b2 modes without the foundation, and (e,f) bar and b3 modes with the foundation.

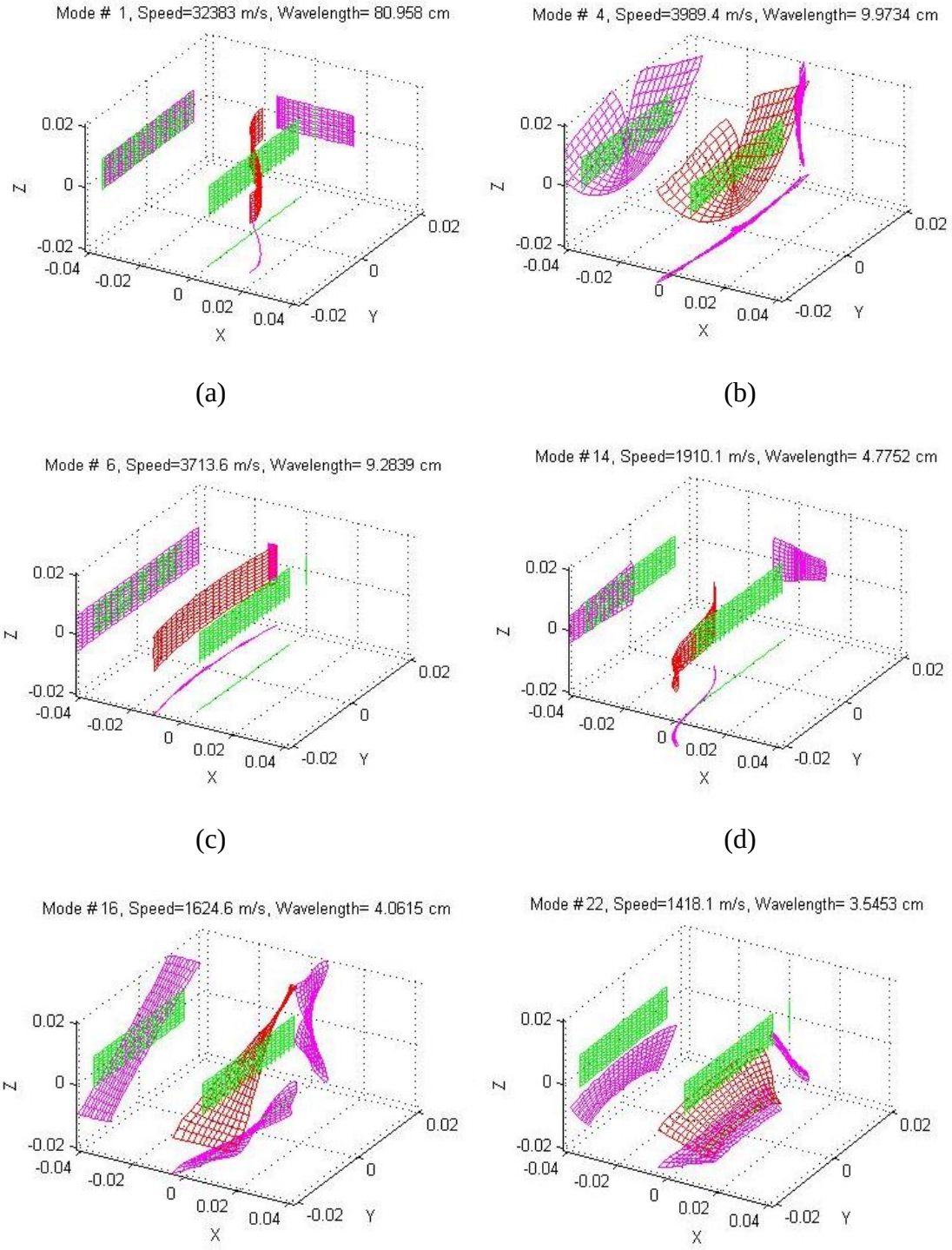

Figure 5.38: The deformation mode shapes at 40 kHz without the foundation: (a) shear, (b) b1, (c) bar, (d) b3, (e) torsion, and (f) b2 mode.

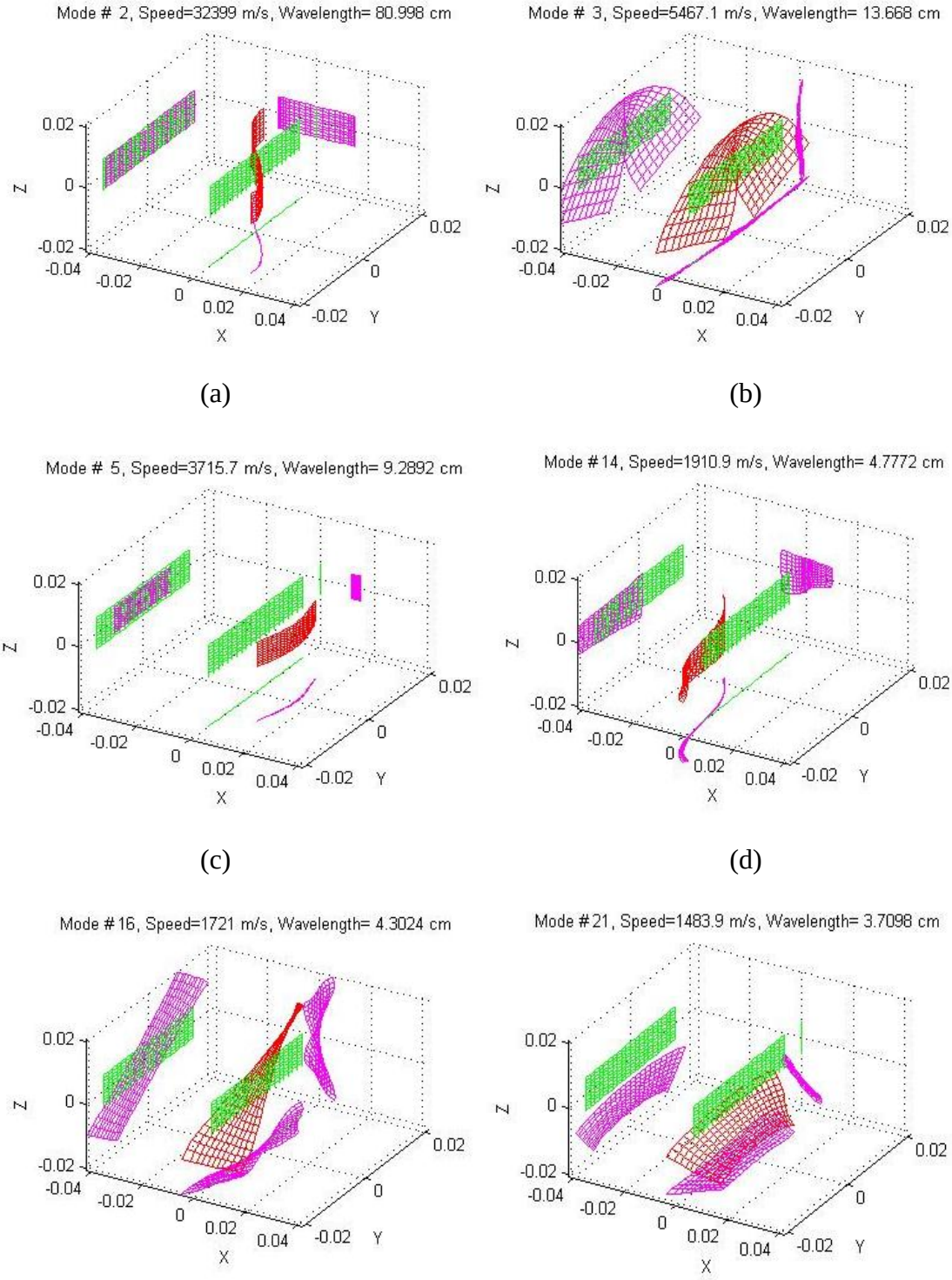

Figure 5.39: The deformation mode shapes at 40 kHz with the foundation: (a) shear, (b) b1, (c) bar, (d) b3, (e) torsion, and (f) b2.

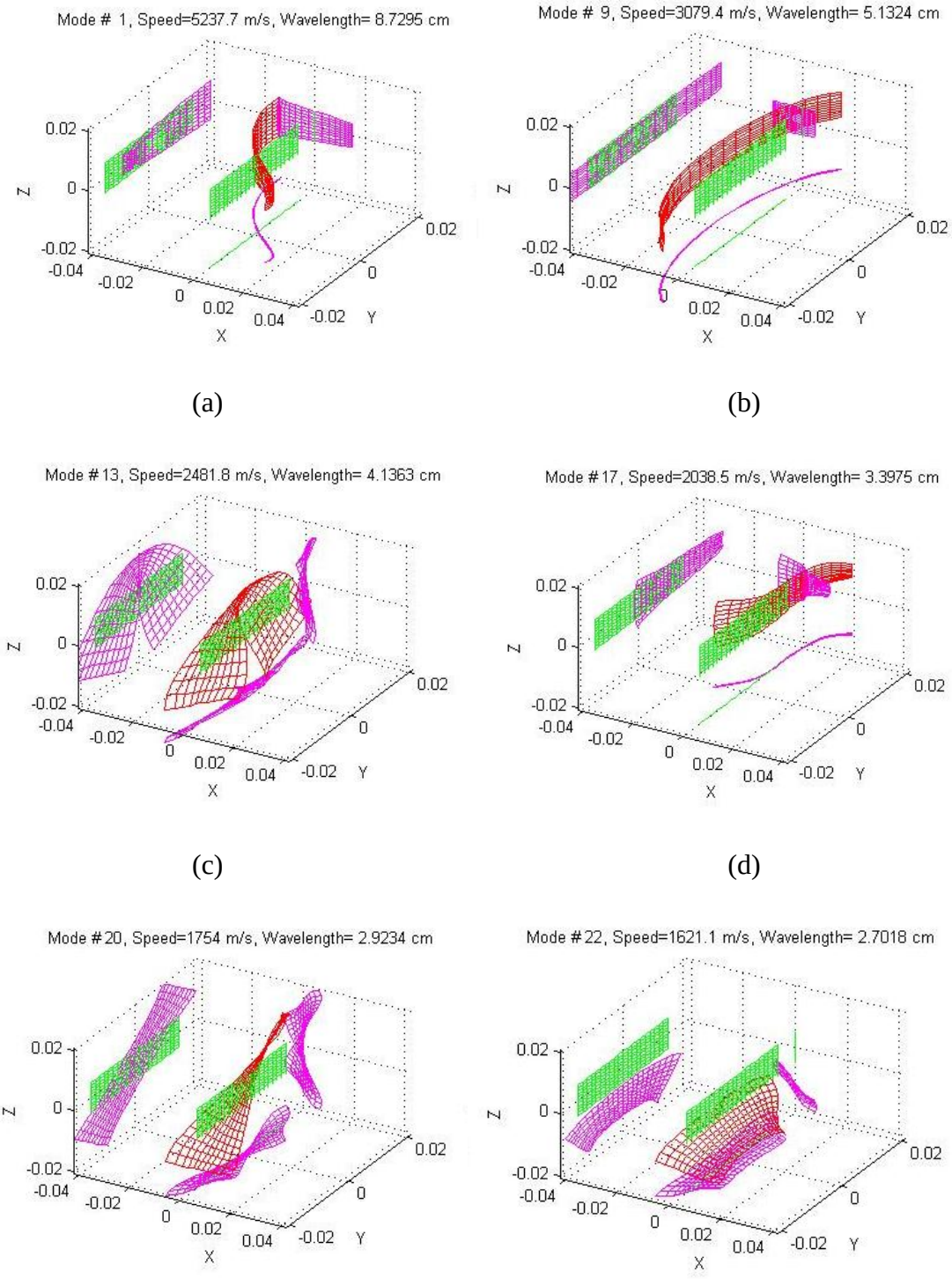

Figure 5.40: The deformation mode shapes at 60 kHz without the foundation: (a) shear, (b) b1, (c) bar, (d) b3, (e) torsion, and (f) b2.

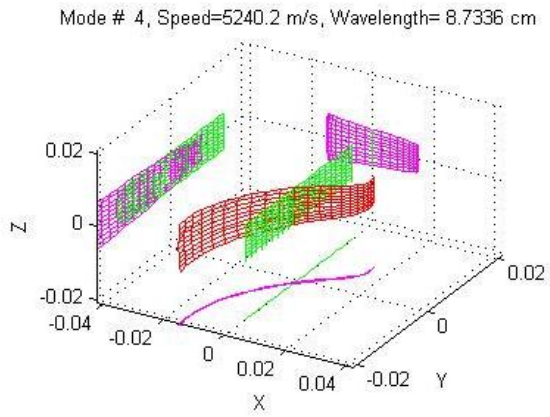

(a)

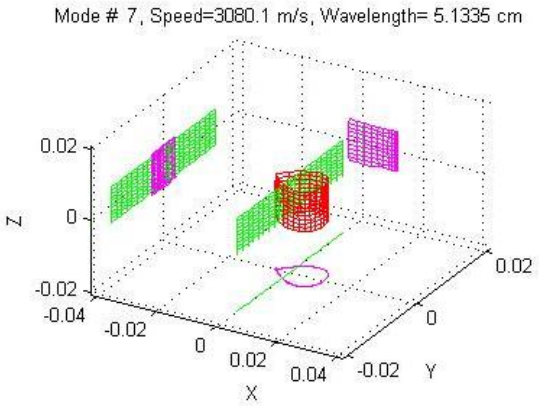

(b)

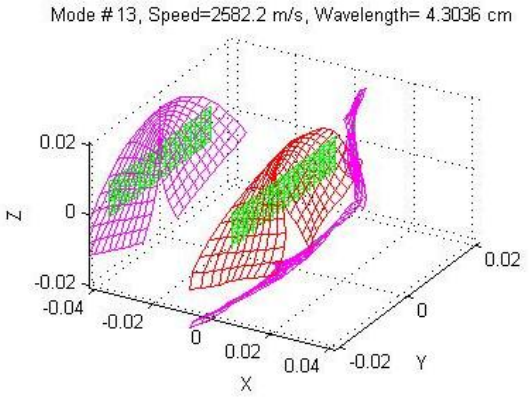

(c)

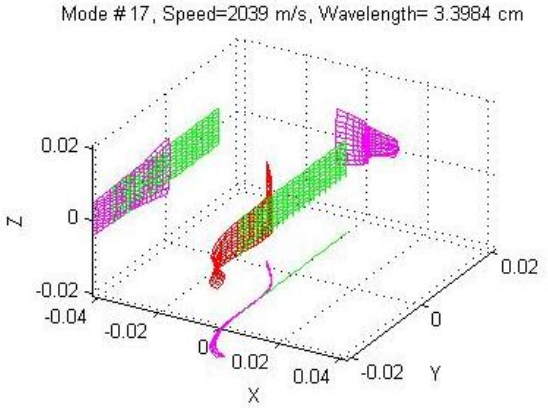

(d)

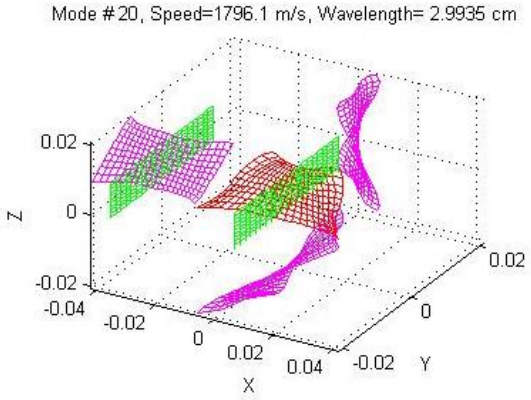

(e)

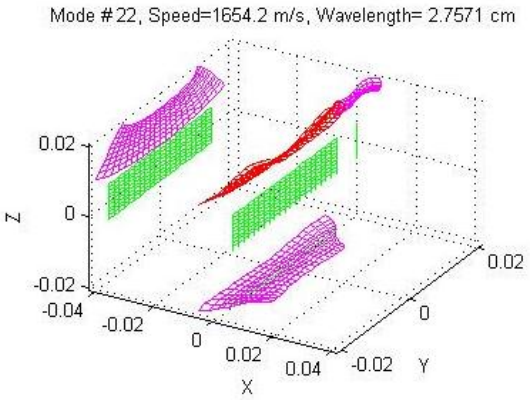

(f)

Figure 5.41: The deformation mode shapes at 60 kHz with the foundation: (a) shear, (b) b1, (c) bar, (d) b3, (e) torsion, and (f) b2.

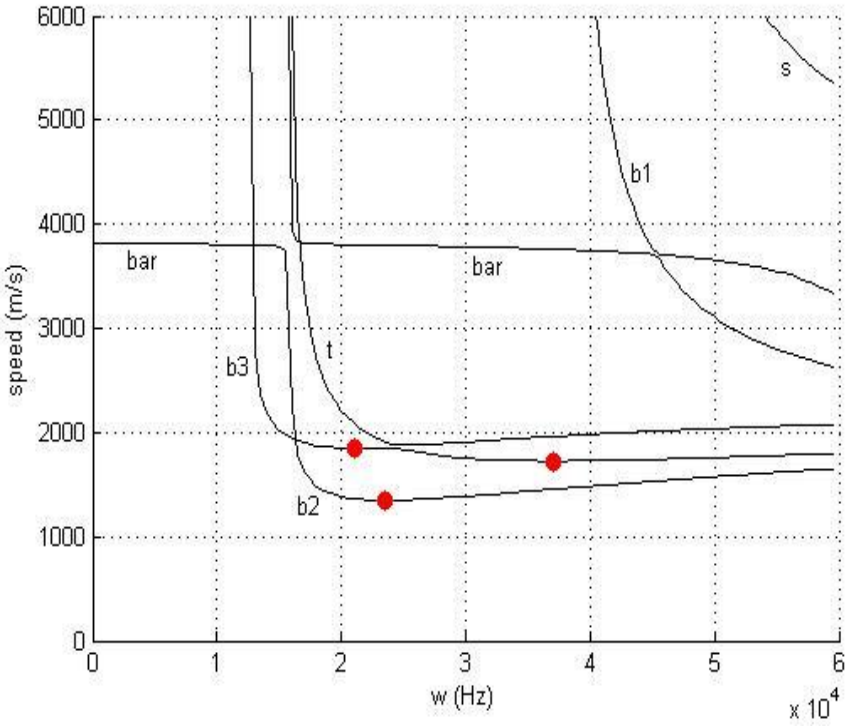

Figure 5.42: Dispersion curves with y and z direction foundations.

The size of cross-section can have dramatic effects on the cross-sectional warpings and thus the three critical speeds. For the most part, the smaller a cross-section the more rigid it behaves. Figure 5.43 shows the dispersion curves for a rail of half the height and width of our nominal IAT rail from Table 5.1 (i.e. a/2, b/2). Figures 5.42 and 5.43 show that the critical speeds of b3, t, and b2 modes decrease from 1852 m/s, 1727 m/s, and 1349 m/s in Fig. 5.42 to 1656 m/s, 1637 m/s, and 1167 m/s in the half-size model. The frequencies of the critical speeds have increased dramatically as well. We can also see that the high frequency mode shapes of b1 and s modes are no longer present and the bar mode is fairly constant at all frequencies since the high-frequency b1 and s modes no longer allow local degrees of freedom to absorb energy. Note that the b1 and s modes still exist but their displacements are negligibly small. All of these agree with our knowledge that smaller cross-sections behave in a more rigid fashion. Conversely for a larger cross-section, we would expect more degrees freedom, and more elastic behavior. Figure 5.44 shows the dispersion curves for a rail cross-section twice the height and width of our nominal model (2*a, 2*b). This time we see the opposite effect. The critical

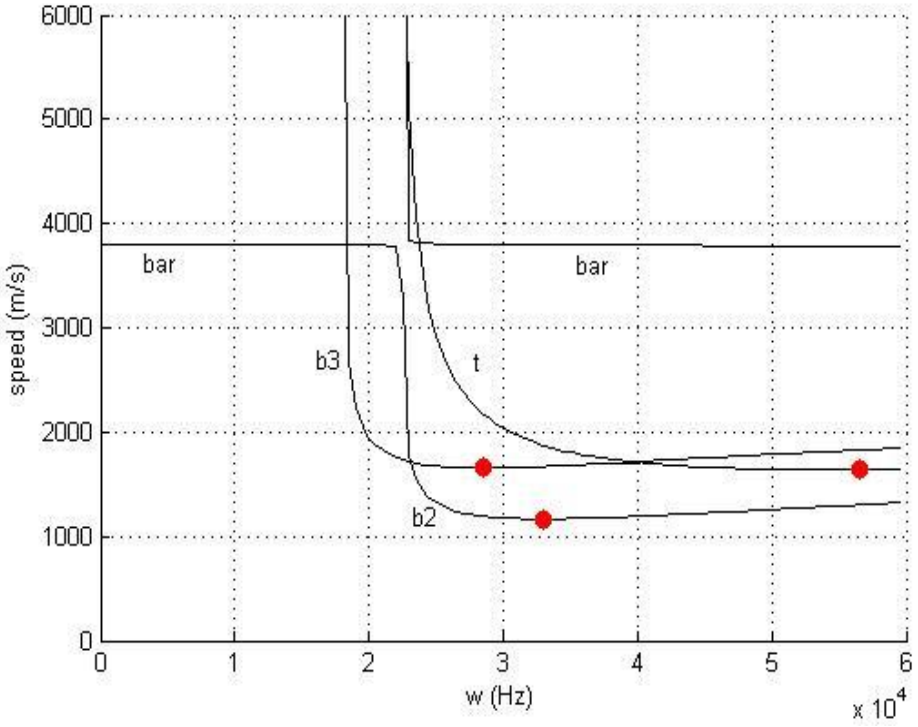

Figure 5.43: Dispersion curve for half the nominal height and width.

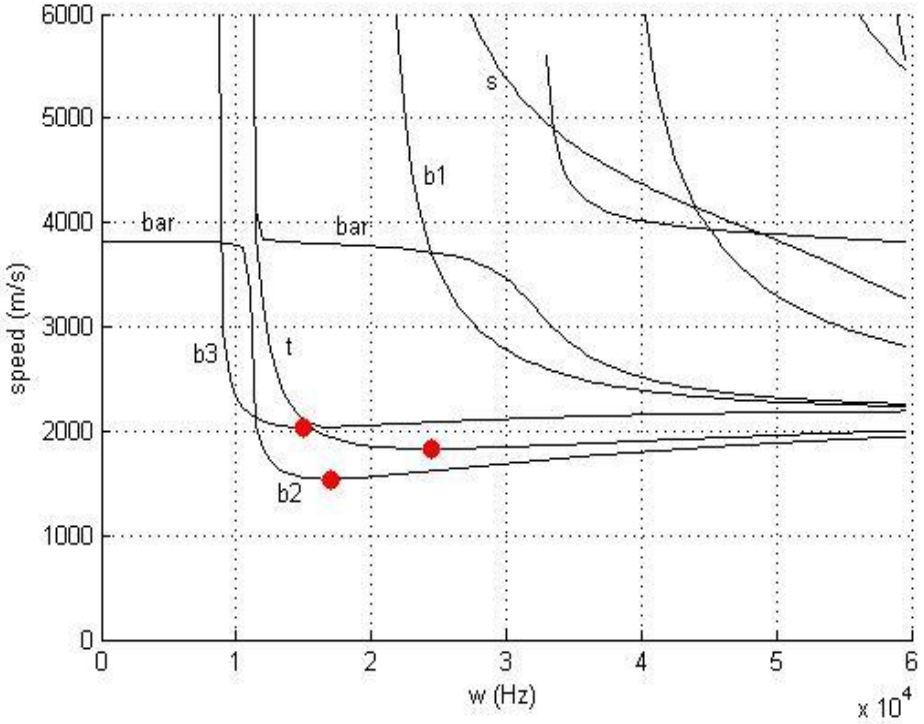

Figure 5.44: Dispersion curve for twice the nominal height and width.

speeds increase to V_{b3} = 2028 m/s, V_t = 1832 m/s, and V_{b2} = 1541 m/s, their corresponding frequencies decrease, and more high-frequency modes exist. We see that in general, as the rail cross-section increases in size the critical speeds will increase while their frequencies decrease, and more high-frequency modes exist.

Further comprehension of the critical speeds includes understanding of their perspective change with respect to variable changes in the rails. Most importantly change in size can either restrain wave speed or introduce more high-frequency modes and local degrees of freedom. Sensitivity of the critical speeds with respect to the cross-sectional size, i.e., the rail width and height can be seen below in Figs. 5.45 and 5.46, respectively. Figure 5.45 shows the three critical speed sensitivities with respect to the rail width. All other dimensions/variables remain the same as those in Table 5.1. From this figure we can see that the rail width has greatest effect on the torsional mode while almost no effect on the b3 mode. This is expected since increase in the width directly affects the inertial properties of a beam under bending. Hence for I= $ab^3/12$, the rail width is the cubic term for the b2 mode and the single term for the b3 mode. Therefore we see much greater sensitivity of the b2 mode with respect to the rail width. The torsional mode on the other

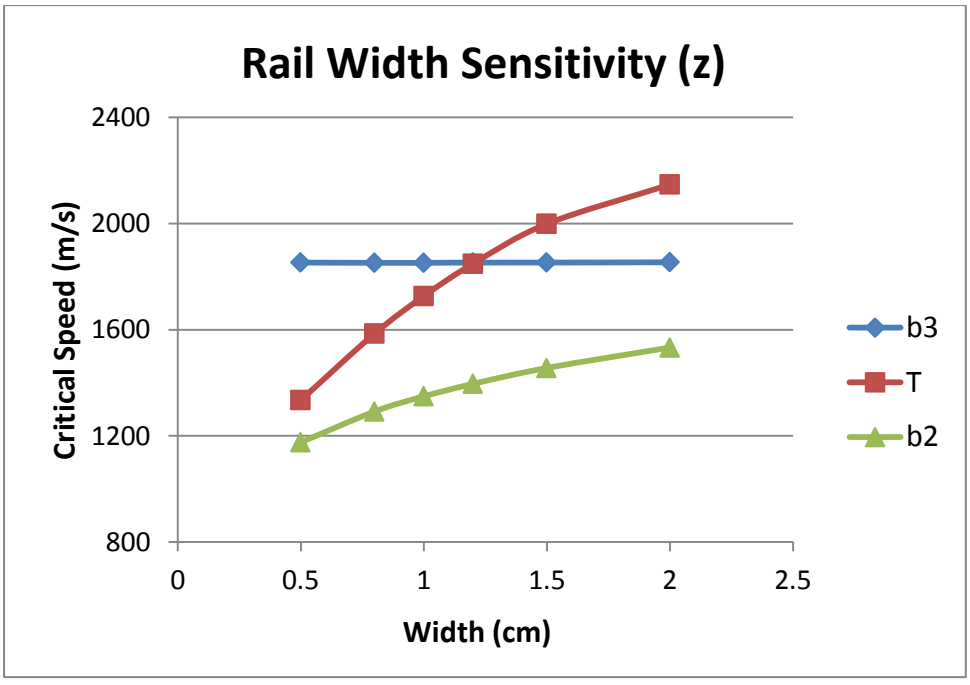

Figure 5.45: Critical speed sensitivity with respect to the rail width.

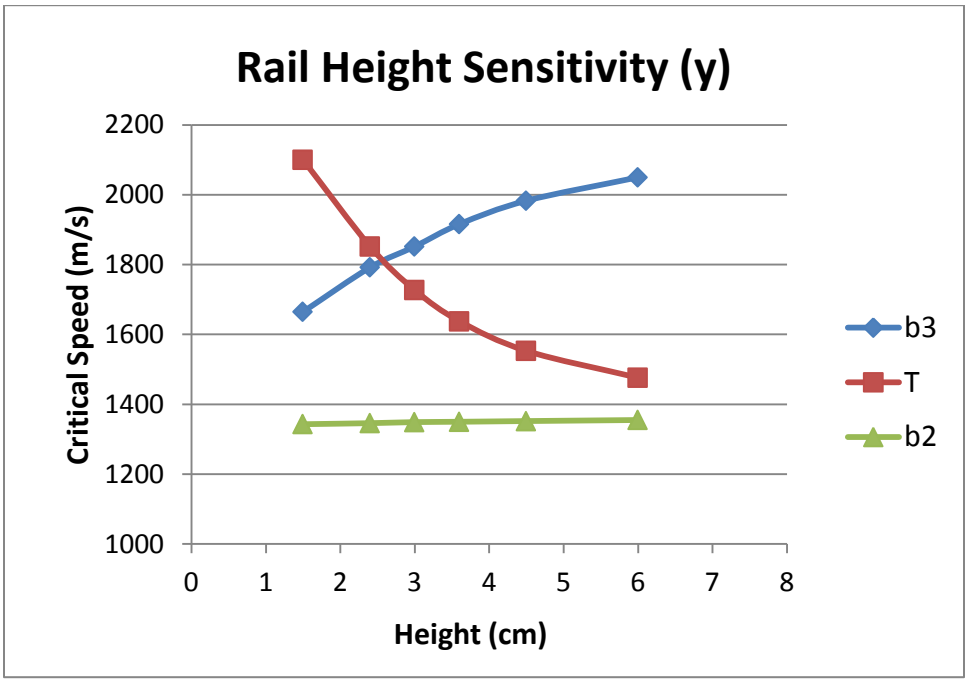

Figure 5.46: Critical speed sensitivity with respect to the rail height.

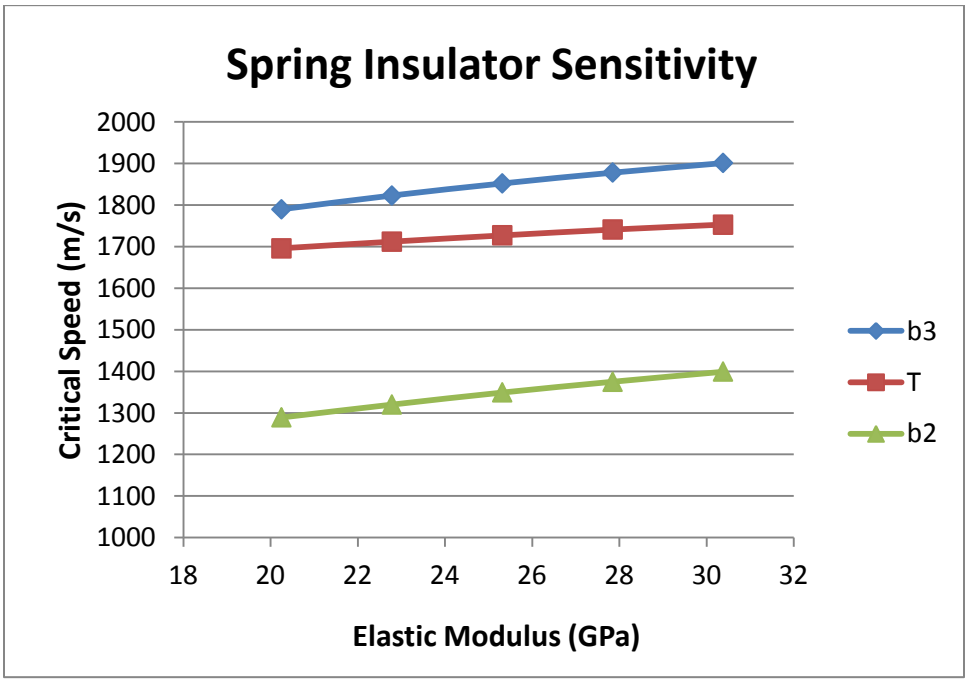

Figure 5.47: Critical speed sensitivity with respect to the spring insulator.

hand changes with the relationship between width and height. The largest torsional modes occur with a height/width ratio of 1 and will decrease as the ratio increases or decreases. Furthermore, Fig. 5.46 shows the critical speeds sensitivity to changes in the rail height. Again the torsional mode is affected the most by changing the height/width ratio (as a/b approaches 1 the critical speed increases), but in this case the variable height is the cubic bending inertial property for the b3 mode and single term in the b2 mode causing greater sensitivity in the b3 mode.

Although we chose to ignore propagating waves with wavelengths under 3 cm, expanding our FEA to find the dispersion curves at high frequencies greater than 100 kHz, we see that all the waves speeds relating to forward propagation converge to a single speed, 2376.8 m/s. Recall that above the shear speed forward wave propagation no longer exist, therefore this represents our shear speed V_{shear}= 2376.8 m/s for our 2D cross-sectional analysis which compares favorably with our Timoshenko model where we have V_{shear} = 2169.6 m/s.

Because the elastic foundation has profound effects on the characteristic speeds of a rail-foundation structure, the elastic modulus of the foundation is introduced here as another sensitivity variable. Figure 5.47 shows the influences of Young's modulus *E*. All three critical speeds change linearly with the elastic modulus, agreeing well with the simplified beam models. The b2 mode has the greatest slope, followed by the b3 and torsional modes. While this is not unsuspected, it should be noted that the spring foundation interacts primarily with transverse motions (e.g., the b2 and b3 modes), while the torsional wave is an internal wave which has more out-of plane displacements than transverse displacements. Therefore we expect the elastic foundation to affect the torsional mode the least.

The effects of temperature are also examined because temperature change can have significant effects on material properties. For example, as the temperature of a material increases the energy in the molecular structure increases and the molecules begin to vibrate more rapidly. This causes the material to become softer. Hence, the elastic modulus of most materials decreases with temperature increase. Figure 5.48 shows the elastic modulus of some common materials over a large temperature range [43]. Our analysis will include the temperature range from 0 to 140 degrees Fahrenheit as this

includes the low temperature range for the possibility of cold firing and the high temperature range around the failure temperature of G10 for repetitive launches. Within our temperature range we can see from Fig. 5.48 that the elastic modulus behaves in a linear fashion, and from the nominal elastic modulus of copper at 70 degrees we have a +3% change at 0 degrees and a -3% change at 140 degrees. The Poisson ratio and density change can be considered negligibly small over this temperature range. The shear modulus changes with the elastic modulus from the simple elasticity equation $G = E / (2*(1+\upsilon))$ [44]. From this we can assume that the internal properties of the rail change linearly and the change of response is also linear. Since the changes are internal to the rail, we can expect the torsional mode to be affected the most as per our reasoning of transverse and longitudinal elasticity above. The temperature sensitivity is shown in Fig. 5.49. This compares favorably with our previous analysis, i.e., the torsion mode is the most affected one, followed by the b3 and b2 modes, respectively. Comparing Figs. 5.47 and 5.49, we can see that the variable in each is an elastic parameter and they behave linearly. Furthermore, the difference between external and internal elasticity can be seen. The external elastic foundation has more influences on the transverse modes b2 and b3 while the internal elastic modulus has more influences on the out-of plane warpings like the torsional mode. The influence of the elastic insulator on critical speeds is linear, and it ranges from greatest to least on the b2, b3, and t modes, respectively. The opposite is true for the elastic modulus: the greatest to least on the t, b3, and b2 modes, respectively. This leads us to believe that the larger the transverse deformation within a mode is, the less the in-plane deformation that occurs. Also, from our previous analysis, transverse deformations occur at low frequencies as they are restrained at higher frequencies unlike the in-plane deformations.

After variable sensitivity analysis it is only logical to examine multivariable sensitivity. Although in some applications the variable sensitivities do not agree well with each other, it was found that our sensitivity analyses could be combined together for quick multivariable changes with accurate results. For that reason, the sensitivity graphs were reformatted below for Figs. 5.50 through 5.53 into ratios of a nominal value for quick reference estimations. Table 5.1 has the nominal reference values. To quickly estimate the critical of a rectangular rail, simply use the ratios of the sensitivity variables

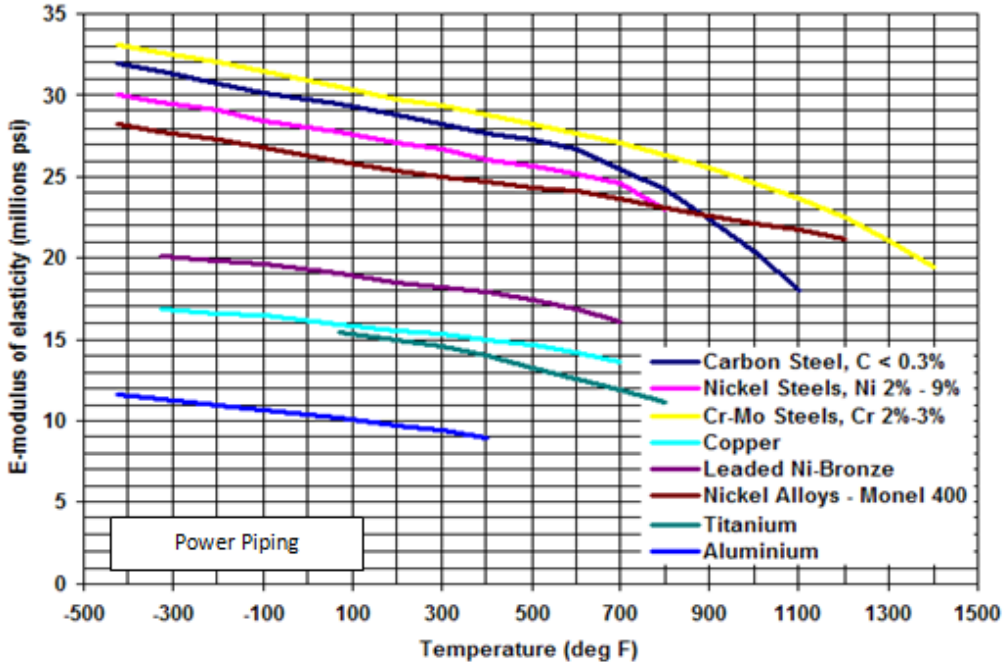

Figure 5.48: Elastic modulus for common metals vs. temperature.

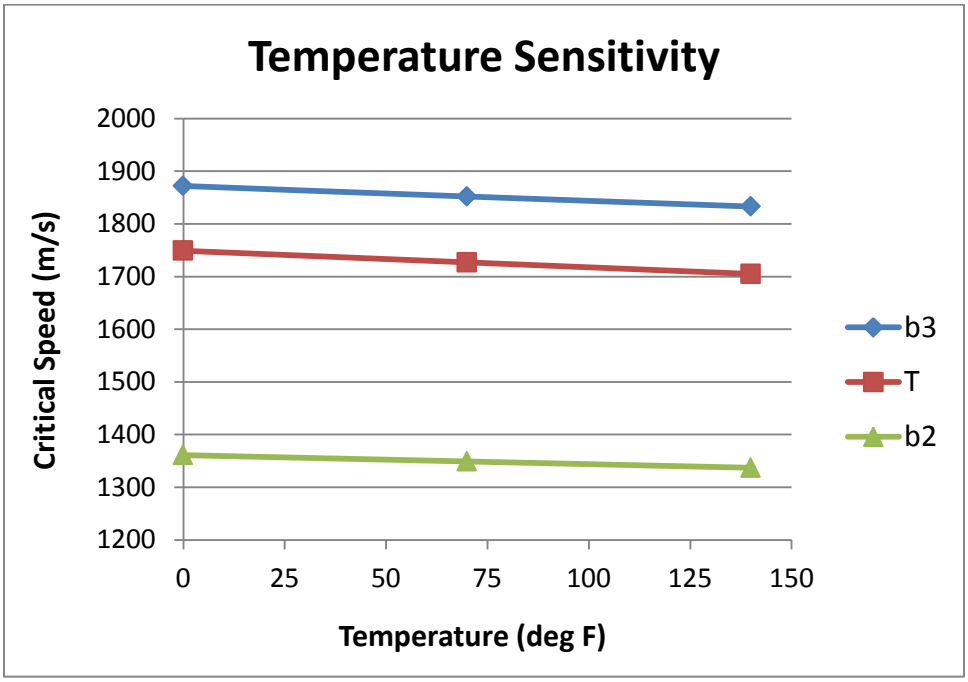

Figure 5.49: Critical speed sensitivity with respect to the temperature.

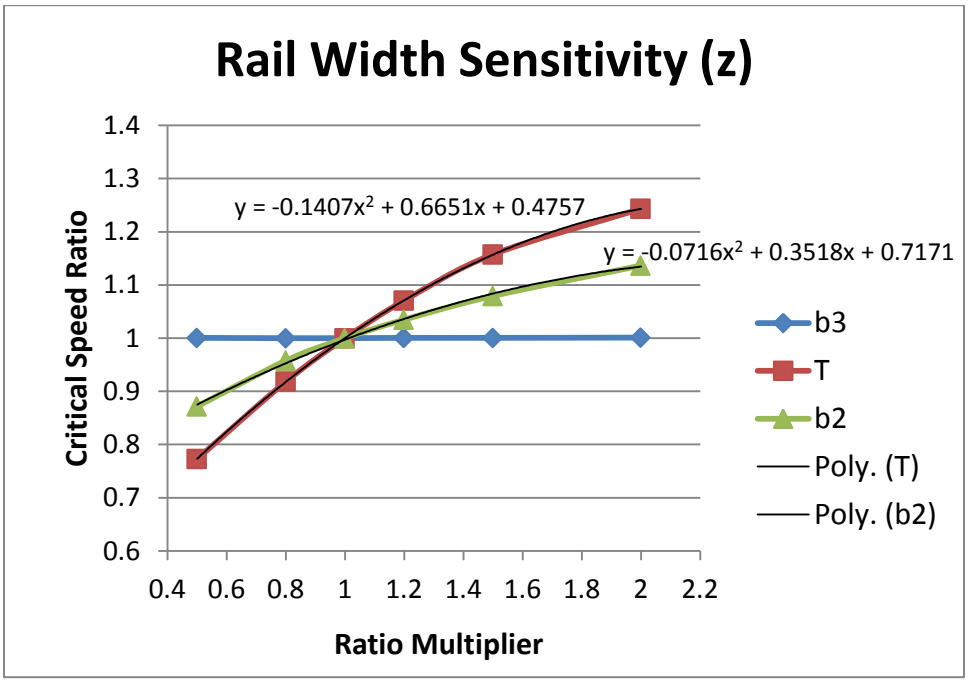

Figure 5.50: Rail width sensitivity for quick reference.

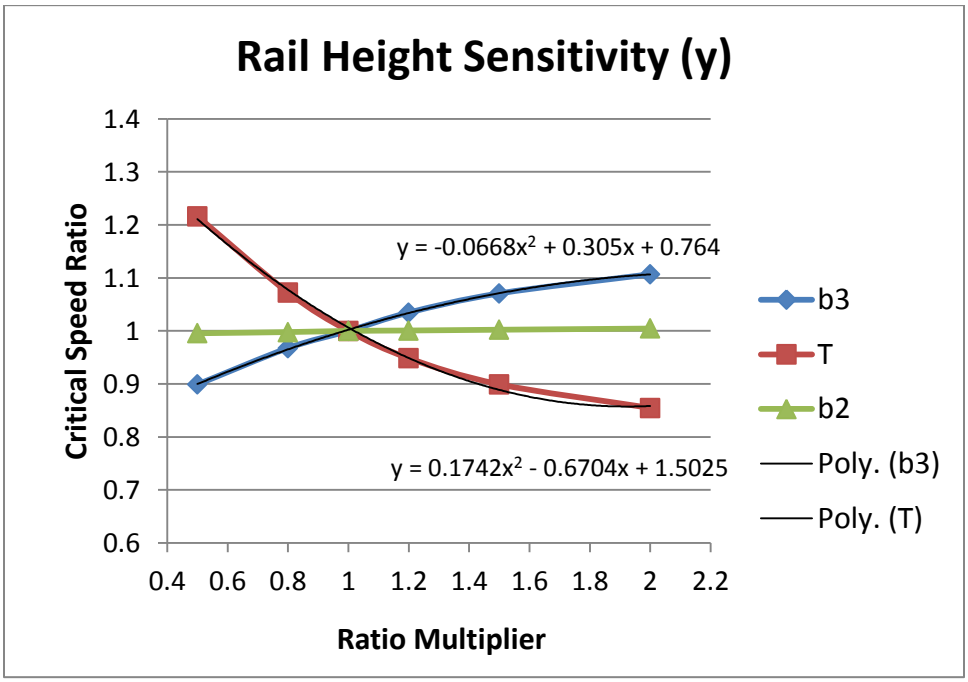

Figure 5.51: Rail height sensitivity for quick reference.

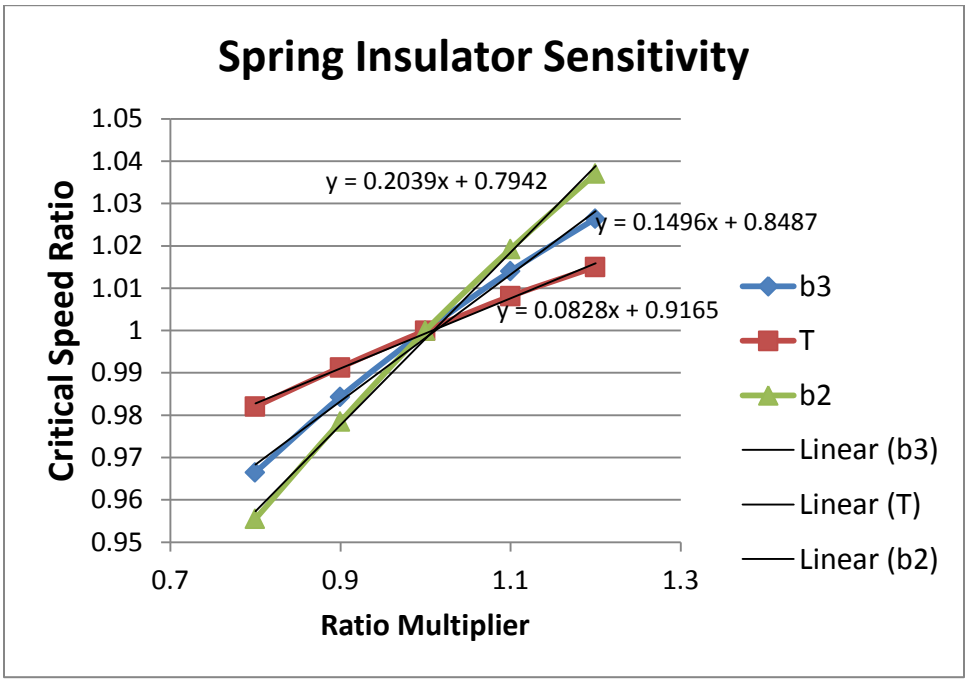

Figure 5.52: Rail insulator sensitivity for quick reference.

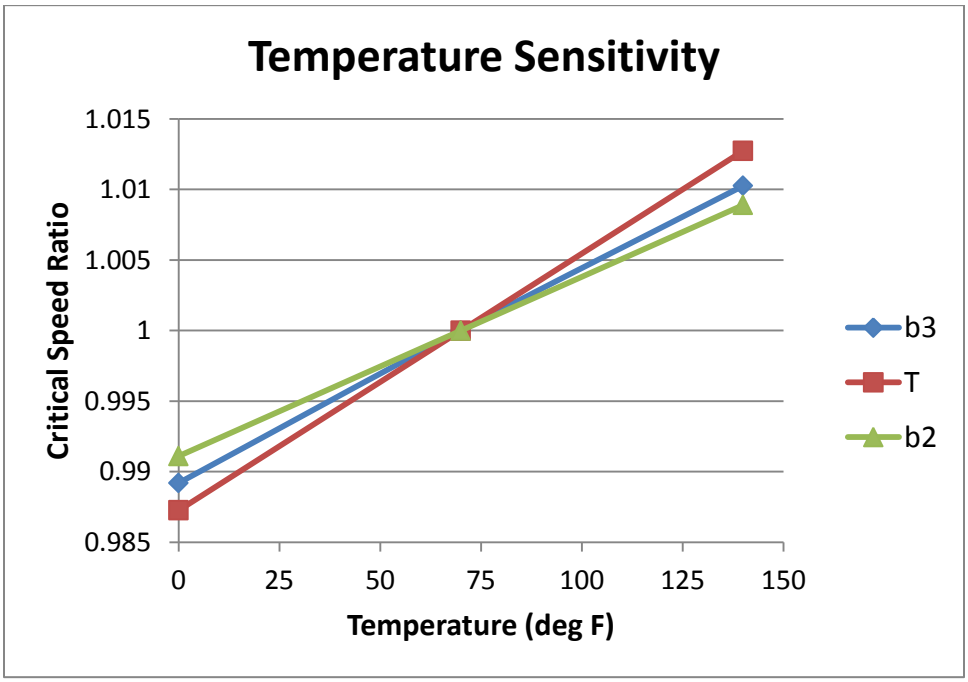

Figure 5.53: Rail temperature sensitivity for quick reference.

Table 5.2: Seven examples of using sensitivity charts.

Example 1		b3	T	b2
0.5*z	**calculated with sensitivity**	1943.95	1276.47	1199.55
1.2*y	**calculated with FEA**	1946	1312	1202
1.1*k	**error**	0.001055	0.027084	0.002035
Example 2		**b3**	**T**	**b2**
0.8*z	**calculated with sensitivity**	1732.01	1670.27	1231.79
0.8*y	**calculated with FEA**	1727	1667	1230
0.8*k	**error**	-0.0029	-0.00196	-0.00146
Example 3		**b3**	**T**	**b2**
1.2*z	**calculated with sensitivity**	1852.86	1722.23	1334.90
1.2*y	**calculated with FEA**	1856	1719	1337
0.8*k	**error**	0.001693	-0.00188	0.001572
Example 4		**b3**	**T**	**b2**
1.1*z	**calculated with sensitivity**	1943.42	1709.60	1399.99
1.2*y	**calculated with FEA**	1923	1713	1402
1.1*k	**error**	0.01062	0.001983	0.001434
Example 5		**b3**	**T**	**b2**
2*z	**calculated with sensitivity**	2052.214	1834.958	1539.818
2*y	**calculated with FEA**	2028	1832	1541
1*k	**error**	-0.01194	-0.00161	0.000767
Example 6		**b3**	**T**	**b2**
1.75*z	**calculated with sensitivity**	1953.53	1847.948	1465.624
1.5*y	**calculated with FEA**	1954	1862	1470
0.9*k	**error**	0.000241	0.007547	0.002977
Example 7		**b3**	**T**	**b2**
.5*z	**calculated with sensitivity**	1665.899	1623.335	1170.769
.5*y	**calculated with FEA**	1656	1637	1167
1*k	**error**	-0.01765	0.008347	-0.00323

to find the corresponding critical speed ratios and multiply them all together. Example, for the b2 mode [(b2 estimate) = (b2 nominal)*(b2 ratio from height)*(b2 ratio from

width)*(b2 ratio from elastic foundation)*(b2 ratio etc.)]. To verify this, seven examples were provided in Table 5.2. Upon inspection, with the exception of the torsional mode in the first example, all the error between the critical speeds calculated by the sensitivity charts and our FEA code are around or under one percent. Therefore these sensitivity charts provide an accurate way to quickly estimate the three critical speeds for a corresponding rectangular rail cross-section within the range of the sensitivity chart variables. As the temperature change has a change on the critical speed on the same order of magnitude as the error (around or under 1%) we can fairly easily assume overall temperature effect as negligible, but the rails themselves during launch are not at a uniform temperature. Therefore, it would be interesting to note that propagating waves will have slightly varying speeds as they travel through the rail. For forward propagating waves the deformation wave will be traveling towards cooler rails at the muzzle, slowing the wave speed. If the temperature variance is large enough we could see larger deformations as some waves begin to catch up and compound on the waves in front of them. We see the same effect in the ocean as the water reaches the shallows before land causing a variance in speed and creating waves.

Next, two other cross-sectional geometries were examined to observe the effects of geometry change. Assuming a similar armature size, a U-shaped rail and T-shaped rail were made to cradle the armature and limit y-direction motion as well as the pitch angle. Using these new geometries with the material properties in Table 5.1, we create two more cross-sectional models from the equations in Chapter 4 to examine the effects on the mode shapes and critical speeds. The cross-sectional view and elemental mesh of the U-shaped rail is shown in Fig. 5.54. Figure 5.55 is the dispersion curve associated with the U-shaped rail. The three critical speeds have changed to V_{b3} = 1980 m/s at 28000 Hz, V_t = 1667 m/s at 28500 Hz, and V_{b2} = 1452 m/s at 21500 Hz. Since we essentially changed the overall size of the rail, we might find that using the overall cross-sectional size and sensitivity charts may compare favorably with these results. Comparing this with an overall size change $b_{eff}=1.5*b_{nom}$ sensitivity chart we see that V_{b3}=1853 m/s, V_t = 1999 m/s, and V_{b2} = 1456 m/s do not compare well with our FEA of the U-shaped rail. On the other hand the results can be explained theoretically using previous ideals. As b3 and b2

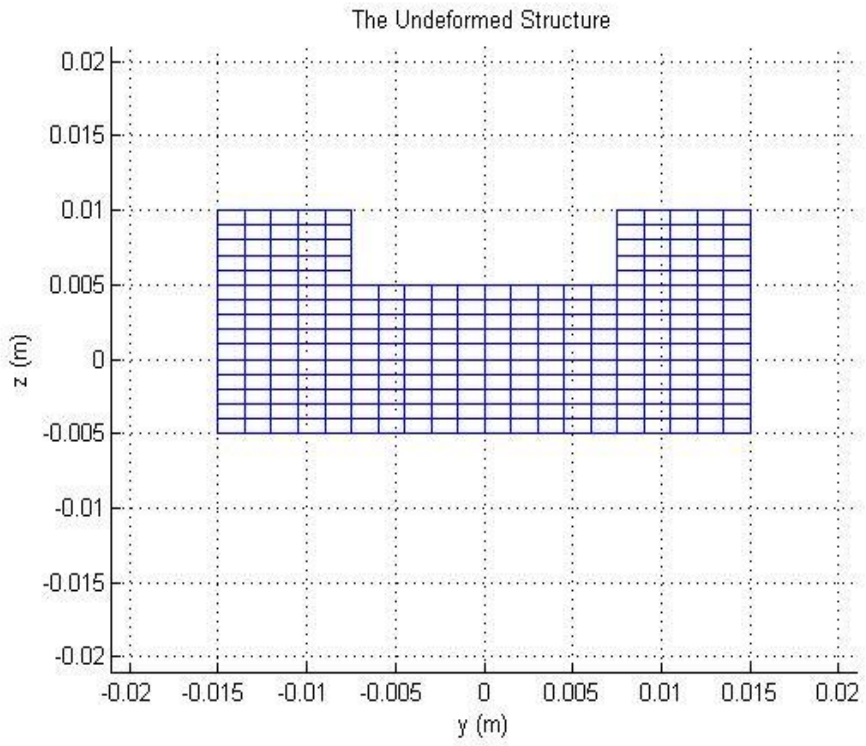

Figure 5.54: U-shaped rail.

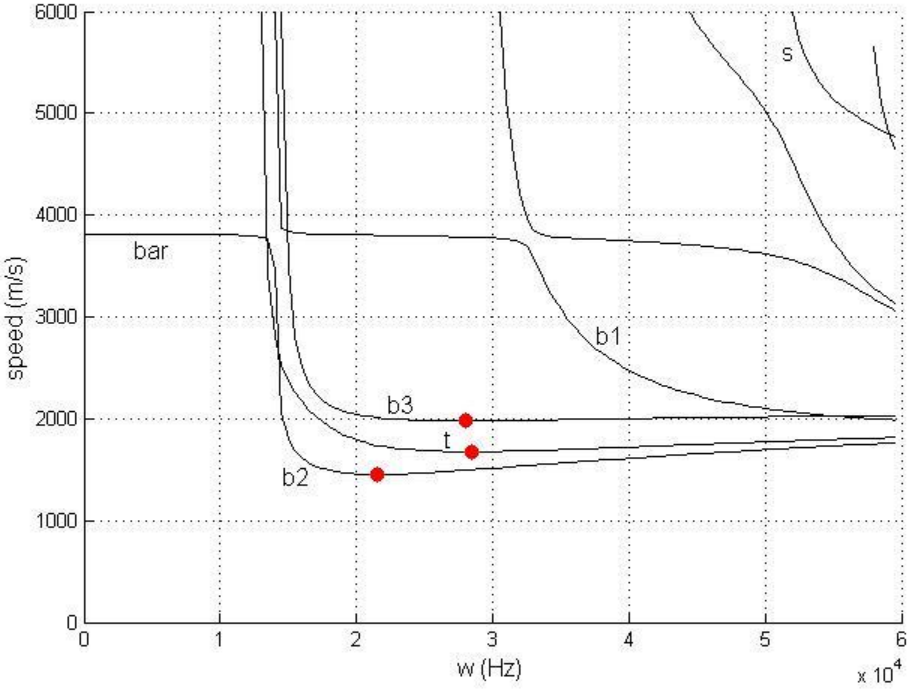

Figure 5.55: Dispersion curve for the u-shaped rail.

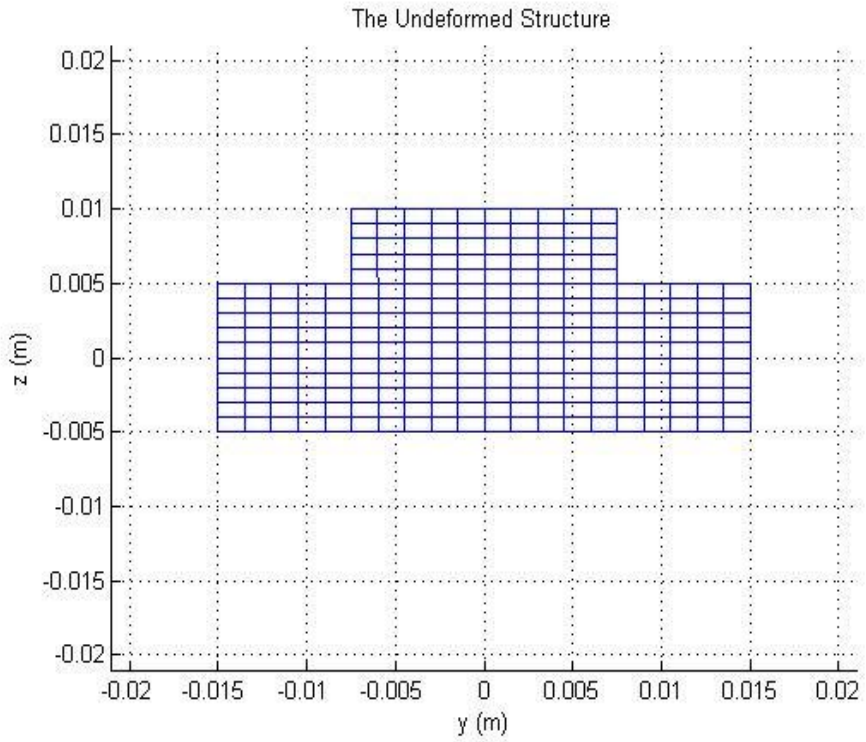

Figure 5.56: T-shaped rail.

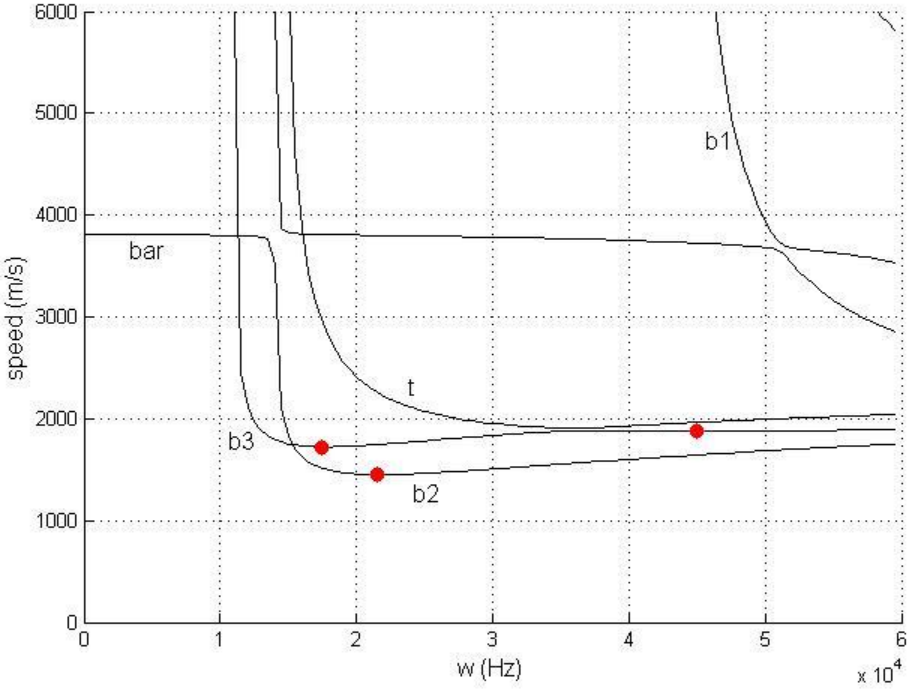

Figure 5.57: Dispersion curve for the t-shaped rail.

modes are bending modes, looking at the bending inertial changes in the U-shaped rails shows that we have increases in both I_z and I_y, therefore we should see resulting increases in the b3 and b2 modes. The U-shaped rail decreases the ratio of height/width towards 1, but the lack of material in the middle of the rail greatly decreases the elasticity of the cross-section under a twisting load. We see a resulting decrease in the torsional critical speed. A similar analysis can be done with the T-shaped rail as well. The cross-sectional mesh is shown in Fig. 5.56 and the dispersion curve is shown in Fig. 5.57. The corresponding critical speeds have become V_{b3} = 1724 m/s at 17500 Hz, V_t = 1875 m/s at 45000 Hz, and V_{b2} = 1451 m/s at 21500 Hz. Again comparing with an overall size change does not provide good results. If we then compare with the U-shaped rail, it can be seen that the bending inertia about the y-axis is the same, and it follows that the associated critical speed of the b2 mode is the same for both models. The z-axis bending inertia decreases in the T-shaped rail and we see a correlation where the b3 critical speed drops to V_{b3} = 1724 m/s. For the torsional critical speed, there is an increase from the U-shaped rail. The material of the T-shaped rail is more towards the middle of the cross-section increasing twisting rigidity and thereby increasing the critical speed associated with the torsional mode.

CHAPTER 6
SUMMARY AND CONCLUSIONS

6.1 Summary

This thesis provides detailed derivations and explanations of the actual causes and physical implications of the three characteristic wave speeds (i.e., critical, shear, and bar speeds), the corresponding waveforms, and their roles in wave dynamics of rail-foundation structural systems like railguns. Moreover, several erroneous derivations and explanations in the literature on characteristic speeds of rail-foundation structures are pointed out. Furthermore, a numerical method for 2D sectional finite-element analysis of cross-sections is proposed, and the influences of cross-sectional in-plane and out-of-plane warpings on characteristic speeds are numerically investigated in detail.

6.2 Conclusions

One-dimensional analysis of a quasi-stationary load moving along an infinite beam on an elastic foundation reveals different waveforms between the three characteristic speeds. Before the critical speed there is a standing wave on the rail. The critical speed is when the moving load starts to resonate with the resulting wave profile and the quasi-stationary buckling load of the rail-foundation system becomes zero. Above the critical speed waves begin to propagate from the armature resulting in an uneven path for the armature to traverse. Between the critical and shear speeds is the only speed region where transverse waves can propagate forward. The bar speed is the highest speed for any elastic wave to propagate within the rail and it happens when the rail behaves like a rigid bar and resonates with the elastic foundation. Therefore no forward waves exist in front of the armature after this speed, but the rail has large waves behind the armature causing rear contacting points of the armature to bounce and impact the rails. It was also found that the shear and bar speeds are determined by the material properties of the rail while the critical speed is be affected by geometrical and external factors. In other words, the critical speed can be changed by adjusting the elastic foundation's Young's modulus or by applying a pretension to the rails. Applying a pretension loading is shown to be able to decrease the speed gap between the critical and shear speeds, thereby decreasing the speed zone of propagating waves. Furthermore bending and shear rotations are coupled in

an acoustic mode (in phase) in front of the armature when the armature speed is below the shear speed, and they are coupled in an optical mode (out of phase) behind the armature when the armature speed is beyond the bar speed. Hence, shear rotation plays an important role in wave dynamics of railguns.

Finite-element analyses of rail cross-sectional planes show the mode shape geometries and their longitudinal wave propagation within the rails. For a rail on an elastic foundation there exist three critical speeds beyond which waves begin to propagate away from the armature; one critical speed is associated with each of the b3, b2, and torsional modes. Size and geometry greatly influence these three critical speeds, but the torsional mode is affected more by internal changes to the rail since it is mainly an out-of-plane deformation. On the other hand, the critical speeds corresponding to the b2 and b3 bending modes are more affected by external properties as they have more in-plane and transverse deformations.

REFERENCES

[1] L. Fryba, Vibration of Solids and Structures under Moving Loads, third ed., Thomas Telford, London, UK, 1999.

[2] J.D. Cinnamon, Hypervelocity Gouging Impacts, AIAA, Reston, Virginia, 2009.

[3] H.D. Fair, Electromagnetic launch science and technology in the United States enters a new era, IEEE Transactions on Magnetics 41(2005) 158-164.

[4] G.A. Shvetsov, P.G. Rutberg, A.V. Budin, Overview of some recent EML research in Russia, IEEE Transactions on Magnetics 43(2007) 99-106.

[5] G.A. Svetsov, V.M Ermolenko, V.D. Kurguzov, G.V. Ivanov, S.A. Anisimov, Structural response of a railgun accelerator, IEEE Transactions on Magnetics 31(1995), 657-660.

[6] L. Tumonis, R. Kačianauskas, A. Kačeniauskas, Evaluation of friction due to deformed behaviour of rail in the electromagnetic railgun: Numerical investigation, MECHANIKA 63(2007) 58-63.

[7] R.A. Muller, R.L. Garwin, B. Richter, Impact Fusion with a Segmented Rail Gun, Los Alamos Scientific Laboratory, July 2010.

[8] J.P. Barber, B. Challita, B. Maas, L. Thurmond, Contact transition in metal armatures, IEEE Transactions on Magnetics 27(1991) 228-232.

[9] J. Barber, D. Bauer, K. Jamison, J. Parker, F. Stefani, A. Zielinski, A survey of armature transition mechanisms, IEEE Transactions on Magnetics 39(2003) 47-51.

[10] A.J. Johnson, F.C. Moon, Elastic waves and solid armature contact pressure in electromagnetic launchers, IEEE Transactions on Magnetics 42(2006) 422-429.

[11] A.J. Johnson, F.C. Moon, Elastic waves in electromagnetic launchers, IEEE Transactions on Magnetics 43(2007) 141-144.

[12] K.B. Lewis, N.V. Nechitailo, Transient resonant dynamics of components in hypervelocity launchers at critical speeds, IEEE Transactions on Magnetics 43(2007) 157-162.

[13] D.J. Laird, The Investigation of Hypervelocity Gouging, PhD thesis, Air Force Institute of Technology, 2002.

[14] R.A. Marshall, C. Persad, A. Jamison, M.J. Maytac, Observation of solid armature behavior, IEEE Transactions on Magnetics 31(1995) 214-218.

[15] J.P. Barber, A. Challita, Velocity effects on metal armature contact transition, IEEE Transactions on Magnetics 29(1993) 733-738.

[16] L. Tumonis, R. Kačianauskas, A. Kačeniauskas, M. Schneider, The transient behaviour of rails used in electromagnetic railguns: Numerical investigations at constant loading velocities, Journal of vibroengineering 9(2007) 15-17.

[17] L. Tumonis, M. Schneider, R. Kačianauskas, A. Kačeniauskas, Structural mechanics of railguns in the case of discrete supports, IEEE Transactions on Magnetics 45(2009) 474-479.

[18] A.J. Johnson, Elastic dynamics of sliding electrical contacts under extreme conditions, PhD thesis, Cornell University, 2008.

[19] L. Tumonis, M. Schneider, R. Kačianauskas, A. Kačeniauskas, Comparison of dynamic behaviour of EMA-3 railgun under differently induced loadings, MECHANIKA 78(2009) 31-37.

[20] S.Y. Wang, The structural response of a rail accelerator, IEEE Transactions on Magnetics 20(1984) 356-359.

[21] A.J. Schoolderman, W.A. de Zeeuw, M. Koops, Electrothermal design aspects of transitioning solid armatures, IEEE Transactions on Magnetics 29(1993) 865-870.

[22] A.V. Metrikine, K. Popp, Steady-state vibrations of an elastic beam on a visco-elastic layer under moving load, Archive of Applied Mechanics 70(2000) 399-408.

[23] Y.H. Chen, Y.H. Huang, Dynamic stiffness of infinite Timoshenko beam on viscoelastic foundation in moving coordinate, Int. J. for Numerical Methods in Engineering 48 (2000) 1-18.

[24] Y.H. Chen, Y.H. Huang, C.T. Shih, Response of an infinite Timoshenko beam on a viscoelastic foundation to a harmonic moving load, J. of Sound and Vibration 241(2001) 809-824.

[25] T. Watt, S. Fish, Explanation of high frequency contact chatter in trailing arm armatures, IEEE Transactions on Magnetics 37(2001) 106-110.

[26] J.T. Tzeng, Structural mechanics for electromagnetic railguns, IEEE Transactions on Magnetics 41(2005) 246-250.

[27] J.D. Achenbach, C.T. Sun, Moving load on a flexibly supported Timoshenko beam, Int. J. Solids and Structures 1(1965) 353-370.

[28] K.F. Graff, Wave Motion in Elastic Solids, Dover, New York, 1975.

[29] F.W. Grover, Inductance Calculations: Working Formulas and Tables, Dover Publication, 1946.

[30] D.J. Thompson, Wheel-rail noise generation, Part III: Rail vibration, J. of Sound and Vibration 161(1993) 421-446.

[31] A.H. Nayfeh, P.F. Pai, Linear and Nonlinear Structural Mechanics, Wiley-Interscience, New York, 2004.

[32] P.F. Pai, M.J. Schulz, Shear correction factors and an energy-consistent beam theory, Int. J. of Solids and Structures 36 (1999) 1523-1540.

[33] S.P. Timoshenko, J.N. Goodier, Theory of Elasticity, third ed., McGraw-Hill, New York, 1970.

[34] W. Flugge, Viscoelasticity, second ed., Springer Verlag, Berlin, 1975.

[35] J.T. Kenney, Steady state vibrations of beams on elastic foundations for moving load, Journal of Applied Mechanics 21 (1954) 359-364.

[36] T.G. Konstantakopoulos, I.G. Raftoyiannis, G.T. Michaltsos, Eigenfrequencies and critical speeds on a beam due to travelling waves, The Open Mechanics Journal 3(2009) 12-19.

[37] L. Gavric, Computation of propagative waves in free rail using a finite element technique, J. Sound and Vibration 185(1995) 531-543.

[38] P.F. Pai, Highly Flexible Structures: Modeling, Computation and Experimentation, AIAA, Reston, Virginia, 2007.

[39] J.V. Parker, D.T. Berry, P.T. Snowden, The IAT electromagnetic launch research facility, IEEE Transactions on Magnetics 33(1997) 129-133.

[40] P.F. Pai, A.N. Palazotto, Two-dimensional sublamination theory for analysis of functionally graded plates, J. of Sound and Vibration 308 (2007) 164-189.

[41] V. Giavotto, M. Borri, P. Mantegazza, G. Ghiringhelli, V.Carmaschi, G.C. Maffioli, F. Mussi, Anisotropic beam theory and applications, Computers & Structures 16 (1983) 403-413.

[42] P.F. Pai, A.H. Nayfeh, A fully nonlinear theory of curved and twisted composite rotor blades accounting for warpings and three-dimensional stress effects, Int. J. Solids and Structures 31 (1994) 1309-1340.

[43] American Society of Mechanical Engineers, ASME B31.1, Power Piping Edition 10, (2010)

[44] C.A. Daniels, Metal Structures and Properties, Abyss Books, 77-105, 140, 2006.